DEEP-LEARNING BASED CLOUD FRACTION RETRIEVAL AND RAINY CLOUD
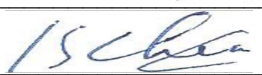CLASSIFICATION USING SATELLITE REMOTE SENSING DATA

by

Qian Liu
A Dissertation
Submitted to the
Graduate Faculty
of
George Mason University
in Partial Fulfillment of
The Requirements for the Degree
of
Doctor of Philosophy
Earth Systems and Geoinformation Sciences

Committee:

_____   Dr. Chaowei Yang, Committee Chair

_____   Dr. Long Chiu, Committee Member
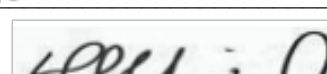
_____   Dr. Paul Houser, Committee Member

_____   Dr. Donglian Sun, Committee Member

_____   Dr. Dieter Pfoser, Department
Chairperson

_____   Dr. Donna M. Fox, Associate Dean,
Office of Student Affairs & Special
Programs, College of Science

_____   Dr. Fernando R. Miralles-Wilhelm, Dean,
College of Science

Date: _____04/08/2022_____   Spring Semester 2022
George Mason University
Fairfax, VA

Deep-learning Based Cloud Fraction Retrieval and Rainy Cloud Classification Using Satellite Remote Sensing Data

A Dissertation submitted in partial fulfillment of the requirements for the degree of Doctor of Philosophy at George Mason University

by

Qian Liu
Master of Engineering
Wuhan University, 2011
Bachelor of Engineering
Wuhan University, 2009

Director: Chaowei Yang, Professor
Department of Geography and GeoInformation Science

Spring Semester 2022
George Mason University
Fairfax, VA

DEDICATION

This is dedicated to my loving husband Hui Xu, my wonderful son Anthony Liu Xiu and my great parents Xiantao Liu and Chunying Zhang.

ACKNOWLEDGEMENTS

TABLE OF CONTENTS

LIST OF TABLES

LIST OF FIGURES

LIST OF EQUATIONS

LIST OF ABBREVIATIONS

Advanced Baseline Imager ....ABI
Advanced Very High Resolution Radiometer .... AVHRR
Averaged Neural Networks...AVNNET
Back-Propagation..BP
Cold Cloud Duration... CCD
Cold Cloud Phase Duration ....CCPD
Climate Prediction Center Morphing Technique ....CMORPH
Contiguous U.S..CONUS
Critical Success Index.. CSI
Cross-track Infrared Sounder ....CrIS
Cloud Top Temperature ....CTT
Decibel Relative to Reflectivity Factor of the Radar... dBZ
Deep Learning... DL
Deep Neural Network ....DNN
False Alarm Ratio ....FAR
Gradient Boosted Regression Trees..GBRT
High Resolution Infrared Radiation Sounders .... HIRS
Integrated Multi-satellitE Retrievals for Global Precipitation Measurement ....IMERG
Liquid Water Path ....LWP
Model Accuracy...MA
Machine Learning ....ML
Moderate Resolution Imaging Spectroradiometer ....MODIS
Multilayer Perceptron Network .... MLP
Near-Infrared..NIR
Neural Networks ....NNET
Probability of Detection .... POD
Probability of False Detection ....POFD
Quantitative precipitation estimation ....QPE
Suomi National Polar-Orbiting Operational Environmental Satellite System ....S-NPP
Tropical Rainfall Measuring Mission .... TRMM
Joint Polar Satellite System JPSS-1

ABSTRACT

DEEP-LEARNING BASED CLOUD FRACTION RETRIEVAL AND RAINY CLOUD
CLASSIFICATION USING SATELLITE REMOTE SENSING DATA

Qian Liu, Ph.D.

George Mason University, 2022

Dissertation Director: Dr. Chaowei Yang

Cloud is the carrier of precipitation and an important atmospheric factor that
influence both the long-term climate change and short-term weather dynamics of the
earth (Molinari and Dudek, 1992; Rossow and Schiffer, 1999; Hamilton, 2006). It
substantially affects Earth's energy budget by reflecting solar radiation back to space and
by restricting emission of thermal radiation to space (Ramanathan et al. 1989), and is
important regulator of the climate and earth-atmosphere system (Sassen et al., 2008). The
profiles and types of clouds are also crucial parameters of global climate models (GCM)
and numerical weather predictions (NWP). They are considered to be the largest
uncertainty in the analysis and prediction of climate change, owning to the difference
between climate models and observational datasets over the area where clouds occur
(Dufresne and Bony, 2008). Cloud features such as cloud fractions and precipitation
capabilities have significant different of impact on the earth system and are related to
various natural disasters. The lack of complete knowledge concerning the complex

interactions among clouds, circulation, and climate hinders our ability to simulate the Earth's climate correctly (Daloz et al., 2018). Furthermore, in the condition of climate change, many cloud-related procedures and changes occur in scales that is smaller than the climate model grids. It is impossible to include these sub-scale processes and their response to increasing temperature in current climate change simulations. As a conclusion, a comprehensive investigation of cloud distribution and classification in high resolution is essential for the research and analysis of the entire Earth system.

Regarding the importance of cloud fraction in the performance of climate models and lack of cloud fraction estimation of hyperspectral IR sounders, a deep neural network model is created to retrieve the cloud fraction within the field of view (FOV) of Cross-track Infrared Sounder (CrIS). To reduce the model input factors without losing spectral information thus increase the retrieval efficiency, principal component transformation is performed on the original CrIS spectrum and sensitivity tests are conducted to determine the best performing combination of PCs as model predictors. During the training procedure, the best-performed iteration and epoch numbers are also tested to avoid over fitting. In general, the cloud fraction retrieved from the proposed DNN model are consistent with truth values calculated from the VIIRS cloud mask product, resulting in a low Mean Square Error (MSE) of 0.021 and a high Pearson correlation coefficient (R) of 0.924.

Regarding the challenge of low spatiotemporal resolutions of microwave (MV) precipitation products and the relative low accuracy of infrared (IR) products, this study combines the information and takes advantages from both MW and IR data. A deep-

learning-based rainy cloud detection and classification framework is developed using ABI spectrum as input predictors and IMERG precipitation estimates as learning target. With the high spatial-temporal resolution of ABI images, the proposed system will be of high performance in real-time regional and local precipitation monitoring. And to include full coverage of precipitation characteristics of the study area, IMERG is used as truth instead of discretely distributed ground observations. The assessment parameters indicate that the proposed models produce relatively accurate results with a critical success index (CSI) of 0.71 and a probability of detection (POD) of 0.86 for rainy cloud detection, and CSI of 0.58 and a POD of 0.72 for convective clouds delineation.

Regarding the relatively low efficiencies of traditional algorithms in processing large remote sensing data, the study utilizes deep learning method to classify rainy cloud types and estimate cloud fractions. With the flourish of Artificial intelligence (AI) and big data techniques, AI methods such as machine and deep learning have been broadly adopted to investigate geospatial and climatological phenomena, as well as predict natural disasters, which triggers a new concept, GeoAI. Although traditional machine learning methods have shown their capability and potential in precipitation detection and monitoring, deep learning (DL) approaches are more accurate in processing big data with large volume and various features (LeCun et al., 2015), such as remote sensing images which contain an abundance of spatial, temporal and spectral information. The study proposes deep-learning based cloud classification and fraction retrieval framework using GEO and LEO satellite data, satellite precipitation product and cloud mask product to detect and classify the rainy clouds of Advanced Baseline Imager (ABI) into stratiform

and convective, and estimate the cloud fractions in the field of views (FOVs) of hyperspectral sounder.

This research is innovative for the following reasons: 1) cloud fractions of hyper-spectral sounders have rarely been addressed but are important for most climate and weather forecast models, this study retrieve the real cloud fraction in each field of view (FOV) of hyper-spectral sounder; 2) most passive microwave (PMW) based satellite precipitation products are at low spatiotemporal resolutions and ground precipitation measurements are sparsely distributed, the study creates a high-resolution rainy cloud type product by combining PMW and geostationary satellite data, to support the precipitation disaster management; 3). After the models are successfully trained, the retrieval and detection results can be produced in high efficiency, which avoids the complex calculation in traditional algorithms; 4). The mature and advanced AI method in the computer science field is utilized to explore new application from the observations from the JPSS and GOES satellites.

CHAPTER ONE INTRODUCTION

Section One Overview and Objectives

Cloud is an important atmospheric factor that influence both the long-term

climate change and short-term weather dynamics of the earth (Molinari and Dudek, 1992;

Rossow and Schiffer, 1999; Hamilton, 2006) with a coverage of 50% of the earth surface.

It substantially affects Earth's energy budget by reflecting solar radiation back to space

and by restricting emission of thermal radiation to space (Ramanathan et al. 1989), and is

important regulator of the climate and earth-atmosphere system (Sassen et al., 2008). It is

found that cloud liquid water path, rainfall, and ocean surface sensible and latent heat

fluxes have a clear dependence on cloud types and scale (Zhang et al., 1999). And due to

their capabilities of producing precipitation (Liu et al., 2019) and mutual influence with

aerosol particles (Xu et al., 2013), the structures, fractions and types of clouds are directly

related to various kinds of atmospheric phenomena (Guzman et al., 2017). Take tropical

cyclones (TC) as an example, the convective clouds embedded in TC systems play an

important role in their sustenance and development, because the intensification and

movement depend on the latent heat released in the clouds (Subrahmanyam et al., 2018).

The fractions and types of clouds are also crucial parameters of climate models and

numerical weather prediction (NWP). They are considered to be the largest uncertainty in

the analysis and prediction of climate change, owning to the difference between climate

models and observational datasets over the area where clouds occur (Dufresne and Bony, 2008). The lack of complete knowledge concerning the complex interactions among clouds, circulation, and climate hinders our ability to simulate the Earth's climate correctly (Daloz et al., 2018). Therefore, the accuracies of model-based reanalysis data sets such as MERRA2 rely significantly on the performance of cloud detection, classification and segmentation. As a conclusion, a comprehensive investigation of cloud fraction and classification are essential for the research and analysis of the entire climatic and atmospheric system. However, it is a challenging task to distinguish different clouds and estimate cloud coverage from satellite imagery because of intraclass spectral variations and interclass spectral similarities (Yu et al., 2018). Additional information from other sources such climate model reanalysis data, as well as a reliable, repaid and accurate methodology are needed to achieve a better result.

Furthermore, many of the atmosphere's most important processes occur on scales smaller than the grid resolution of current climate models. Physical processes relevant to cloud coverage, formation and life cycle can occur at scales as small as a few hundred meters and play a crucial role in determining the Earth's climate by transporting heat and moisture, reflecting and absorbing radiation, and producing rainfall. It is impossible to include physical processes of these sub-scale processes in current climate change simulations. To represent the effects of such sub-grid processes on the resolved scales, physical approximations—called parameterizations—have been heuristically developed and tuned to observations over the last few decades. However, owing to the sheer complexity of the underlying physical system, significant inaccuracies persist in the

parameterization of clouds and their interaction with other processes, such as boundary-layer turbulence and radiation (Stevens et al., 2013; Bony et al., 2015; Schneider et al., 2017). Therefore, sub-grid parameterization development is crucial to improve climate predictions (Rasp et al., 2017) and climatological applications.

Among all the clouds, rainy cloud is critical for monitoring hydrological disaster, studying precipitation and water science, and developing climate model, however, there is no high resolution near-real-time rainy cloud product to support these studies. This dissertation proposes to fill this gap using deep learning methods to automatically classify rainy cloud in to convective, stratiform and non-rainy at 2km spatial resolution and 5 min temporal resolution using GOES-16 Advanced Baseline Imager (ABI) data. The results of this study will provide near-real time decision support for the warning and mitigation of natural disasters such as tropical cyclones and storms. The AI model will also help to increase the accuracy and efficiency compared to traditional detection methods. In light of the aforementioned aspects, this dissertation focuses on the following aspects:

1). Fusion of different datasets sources. The input predictors and learning targets of the models proposed in this research have different spatiotemporal resolutions, data structures and storage formats. To integrate these datasets into the same AI models (rainy cloud classification and cloud fraction retrieval models), corresponding predictors and learning target should be preprocessed including initial quality control and spatiotemporal collocation. For cloud fraction retrieval, CrIS fields of view are collocated with VIIRS cloud mask; for rainy cloud classification, GOES-16 ABI pixels are collocated with IMERG grids.

2). Building a DNN model for cloud fraction retrieval in hyperspectral sounder FOVs using CrIS spectrum information and VIIRS cloud mask. Under the full spectral resolution mode, the CrIS measures 2211 radiance channels in total. If these original channels are all adopted as input predictor, the model efficiency will be significantly reduced. In order to retain all the spectral information of the channels and improve the calculation efficiency, the CrIS spectrum are firstly transferred to principal components (PC). Then the optimized PC number is determined through a series of sensitivity tests. The cloud fraction retrieval model is trained using these selected PC and VIIRS pairs. Model parameters such as iteration and node numbers are tuned to achieve optimized performance. To further validate the model accuracy, a set of independent data and use cases are tested.

3). Building a deep-learning based rainy cloud detection and convective pixel delineation framework based on DNN model using GOES-ABI and IMERG precipitation estimate. The framework contains two models, a rainy cloud detection model which detect the pixels with rainfall rate > 0.1mm/hour; and a convective cloud delineation model which segment the pre-detected rainy clouds into convective and stratiform clouds. The input predictors are selected based on the knowledge of spectral features of cloud types. The performance of different machine-and deep-learning methods will be compared to confirm the superiority of the proposed DNN models.

4). Exploring the feasibility of AI methodologies in natural phenomena analytics using cloud features as examples.

Section Two Cloud Fraction Retrieval

Cloud fraction is defined as the proportion of cloud coverage in a satellite pixel or a weather or climate model grid box. It is one of the most crucial cloud parameters in modeling the downward radiation at both the Earth's surface and at the top of the atmosphere (Dürr and Philipona, 2004; Chen et al., 2012), and also one of the largest sources of uncertainty in Global Climate Models (Mueller et al., 2011; Wang et al., 2019). Since cloud fraction is a key factor in the climate models (Sekiguchi et al., 2003; Chuang et al., 2012), an accurate and reliable cloud coverage estimation is essential for climate studies.

Among all the satellite data, infrared sounder is an important source of Global Climate Model (GCM) and Numerical Weather Prediction (NWP). Different cloud fractions have different effects on the atmospheric radiative transfer. Therefore, the quality of cloud fraction estimation is crucial for the accuracy of the predictions. There are generally three types of cloud fraction retrieval method for infrared sounders. The first one is using visible and infrared channels of satellite sensors to decide the cloud coverage based on the spectral features of cloudy pixels (Arking and Childs, 1985;). Another method is to estimate the effective cloud fraction by simulating the reflectance and transmittivity of cloudy/clear sky using window channel spectrum (Koelemeijer et al., 2001; Sihler et al., 2020). The third method is based on collocated data pairs and use the cloud mask of higher resolution data to decide the cloud coverage of lower resolution data (Huang et al, 2010).

Due to the low spatial resolution of infrared sounders, the last method is widely used based on the correspondence between infrared sounders and their same-platform imagers. Even though promising results have been achieved when using the imager's information to identify infrared sounder's cloud contamination, most of these results have mainly focused on the cloud and clear sky differentiation. The imager's capability in checking sounder's sub-pixel cloud coverage has not been well discussed and explored. With the rapid development of AI technologies, we now have more tools to conduct the cloud investigations. Therefore, this paper innovatively develops a DNN model to automatically estimate the cloud fraction in hyperspectral infrared sounder FOV observations, using the CrIS instrument as an example. The cloud mask of VIIRS, a high-resolution imager onboard the same satellite platform with CrIS, is utilized as the truth to determine the cloud fraction in CrIS FOVs during the model training procedure. It is worth to note that the proposed method could be easily adopted by other hyperspectral infrared sounders. For example, AIRS could be trained using Moderate Resolution Imaging Spectroradiometer (MODIS) measurements, or IASI with Advanced Very-High-Resolution Radiometer (AVHRR). The results from this study can be further used in partial cloud detection and improving other cloud parameter retrievals as well as climate models.

Section Three Rainy Cloud Classification

Precipitation is one of the most essential contributing factors to global hydrological circulation (Campoy et al., 2013) and destructive natural disasters globally including hurricanes, floods, and droughts. Convective precipitation with abnormal

activities of convective systems may lead to severe urban floods (Mason et al., 2009),

landslides (Keefer et al., 1987), and flash floods (Alfieri et al., 2015), which cause

devastating short-term and long-term impacts on people, economies, infrastructure, and

ecosystems. To mitigate these negative impacts, precipitation detection and convective

precipitation extraction data with high spatiotemporal resolution are essential in extreme

precipitation monitoring, forecasting, and early warning systems. These data are also

crucial for validating results and diagnosing problems in numerical weather forecast.

Recently the increasing availability of high spatiotemporal resolution datasets is

contributing to the real-time detection and monitoring of precipitation events in a limited

fashion for various domains, including environmental science (Valipour, 2016), climate

change (O'Gorman, 2015), the economy (Wang, 2018), and society (Skofronick-Jackson

et al., 2017). For example, rain gauge data provide accurate measurements of

precipitation rate (Karbalaee et al., 2017) while their discrete distributions are limited in

both space and time. Passive Microwave (PMW) remote sensing is a widely-used

technique to retrieve precipitation rate but is restricted in spatial-temporal resolutions and

time effectiveness, limiting its resolution in fine-scale disaster warning and real-time

precipitation monitoring. In contrast, optical sensors onboard geostationary satellites

offer higher spatial and temporal resolutions (Hong et al., 2017). The available spectral

information and resolutions for extracting the properties of rainy clouds (e.g., cloud top

height, cloud top temperature, cloud phase, cloud water path (Thies et al., 2008)) are

increasingly more accurate. Infrared (IR) data are more widely used in authoritative

precipitation products including the Tropical Rainfall Measuring Mission (TRMM) 3B42

(Huffman et al., 2007), Integrated Multi-satellitE Retrievals for Global Precipitation

Measurement (IMERG) (Huffman et al., 2015), and Climate Prediction Center Morphing

Technique (CMORPH) Global Precipitation Analyses (Joyce et al., 2004). Given the

advantages of optical sensor data, this paper focuses on rainy cloud detection and

convective precipitation delineation using images of IR and the visible spectrum

CHAPTER TWO LITERATURE REVIEW

<u>Section One Cloud Fraction Retrieval</u>

Traditionally, cloud parameters including cloud coverage in satellite FOVs can be estimated using the spectral information of visible and infrared channels, by calculating the reflection and transmission properties of cloud layers (Arking and Childs, 1985). Another method is developed to simultaneously retrieve the affective cloud fractions of Global Ozone Monitoring Experiment (GOME) pixels by simulating the spectrum of cloudy or partially cloudy pixels based on three ~1-nm-wide wavelength windows (Koelemeijer et al., 2001).

Measurements from satellite infrared sounders provide valuable information for atmospheric profile retrievals, such as temperature, humidity, clouds, green gases, and so on. They are also directly assimilated into numerical weather prediction models (Jones et al., 2017; Li et al., 2016) and General Circulation models (Aumann et al., 2009) for weather forecasting, understanding the climate, and forecasting climate change. By design, the infrared sounders have a large footprint (greater than 10 km in diameter), resulting in their field of views (FOVs) often containing clouds, which can affect the atmospheric window channels. Many infrared sounder-based cloud cover retrieval algorithms have been developed in the past decades (McNally and Watts, 2003; Susskind et al., 2003; Smith and Taylor, 2004; Li et al, 2004; Eresmaa, 2013; Kahn et al., 2014;

Wang et al., 2014; Lin et al., 2017; Liu et al., 2020) for different purposes. A widely used cloud cover retrieval method was developed by Susskind et al., 2003, 2006, 2011, 2014, for the Atmospheric Infrared Sounder (AIRS). In this retrieval method, the clear and cloudy observations are first identified using a cloud clearing method (Susskind et al., 2003). Later, the difference between the radiance of the satellite observations and that of selected channels in the model fit is used to estimate the effective cloud fraction. Assuming the cloud emissivity is spectrally flat, channels are selected that are most sensitive to clouds. This cloud cover retrieval method has been adopted in the AIRS cloud products (Kahn et al., 2014) and been further extended to the Infrared Atmospheric Sounding Interferometer (IASI), as well as the Cross-track Infrared Sounder (CrIS) (Susskind and Kouvaris, 2017; Christopher et al., 2021). It must be noted that the retrieved effective cloud fraction is the product of geometric fractional cloud cover and the cloud emissivity, rather than the real spatial cloud fraction within a sounder's FOV (Kahn et al., 2014), as it is difficult to accurately distinguish them using sounder measurements alone.

In addition to these approaches, the cloud coverage information of the hyperspectral infrared sounders can also be obtained from an accurate collocated imager. Li et al. (2004) developed an effective AIRS cloud detection method based on the cloud mask measured from MODIS. In their study, each AIRS FOV is separately checked by its collocated MODIS cloud mask to determine whether it is cloudy or not. Similar methods also have been developed for the IASI (Eresmaa, 2013) and the CrIS (Wang et al., 2014; Wang et al., 2016) instruments. Since the sounder's cloud information is obtained from

the high spatial resolution (usually around 1 km) imager, the sub-pixel, or partially cloud detection, as well as the cloud fraction retrieval for the infrared sounders becomes available. However, it usually takes a considerable amount of data, time, and computational resources to complete their spatiotemporal data collocation. To solve this issue, Liu et al. (2020) recently developed a novel CrIS cloud detection method based on the deep neural network (DNN). Deep neural network is one of the most widely used artificial intelligence (AI, Antun et al., 2020) and big data technologies (Yang et al., 2019) in the analytics of atmospheric phenomena (Liu et al., 2019; Schlef et al., 2019). Unlike all of the previous mentioned methods, the CrIS spectra are directly trained with VIIRS cloud mask for fast and accurate sounder cloud detection. After the DNN model is constructed, only the CrIS spectra is needed to determine its cloudy scene, avoiding the complex sounder-imager collocation pre-processing.

Section Two Rainy Cloud Classification

Rainy cloud detection is more complicated than merely extracting the cloud area, especially when different types of rainy clouds overlap. There are mainly two types of clouds that produce precipitation - nimbostratus and cumulonimbus clouds (Jensenius, 2017; WMOI, 2019). A nimbostratus cloud is morphologically textureless, usually with a thick layer distributed from low to mid-level altitude. In the daytime, it often looks grey or dark as observed from the ground. This kind of cloud typically produces light or moderate precipitation of longer duration (i.e., stratiform precipitation). When the atmosphere is unstable enough to allow for significant vertical growth of a cumulus

cloud, cumulonimbus clouds form (Donald, 2018). This type of cloud also has typically low base heights at about 300 meters but with tops reaching 15 km. Cumulonimbus clouds produce more substantial and more intense precipitation than nimbostratus clouds, usually along with thunder and lightning due to the collisions between charged water droplets, graupel (ice-water mix), and ice crystal particles.

Different kinds of rainy clouds have characteristic signatures in both reflectance and brightness temperature (BT). Rainy-cloud types are identified using properties that reflect these features, such as cloud height, optical thickness, cloud top temperature, and particle size. For example, differentiating rainy clouds from the non-rainy clouds is achieved using their lower temperature in IR spectrums and unique color and brightness in the visible (VIS) spectrum. Adler and Negri (1988) estimated both tropical convective precipitation and stratiform precipitation from satellite infrared data based on a brightness temperature threshold method. The estimation of precipitation volume can also be achieved by measuring the cloud's time at a specific critical threshold temperature or Cold Cloud Duration (CCD) (Milford and Dugdale, 1990). To improve the CCD method in estimating convective precipitation, Lazri et al. (2014) proposed the Cold Cloud Phase Duration (CCPD). Using a thresholding approach, Arai (2016) detected rainy clouds with visible and thermal IR imageries of AVHRR data and compared the results with radar data for validation. Tebbi and Haddad (2016) trained a support vector machine (SVM) classifier using the BTD spectral parameters of Spinning Enhanced Visible and Infrared Imager (SEVIRI) to detect rainy clouds and extract convective clouds in the northern border of Algeria, and validated the results using observations from rain gauges. Using

SEVIRI data in northern Algeria, Mohia et al. (2017) trained a classifier based on the artificial neural multilayer perceptron network (MLP). Improved from AVHRR and SEVIRI, the new generation Advanced Baseline Imager (ABI) was developed with higher spatial, temporal, and spectral resolutions. The ABI provides images with more thermal and spectral bands and visible colors and brightness, resulting in more sensitive and accurate detection of different kinds of clouds. The high scanning frequency of ABI also allows expedient reactions to the precipitation related disasters, which is essential for the coastlines of the U.S. East Coast study area.

On the other hand, the existence of rainy and convective clouds can be reflected by precipitation products and measurements. Global rain gauge data observe the rainfall rate from the Earth surface and provide available precipitation measurement routinely all over the world. However, these rain gauges distribute sparsely in many important regions such as the mountainous area and cannot be installed and operated over the oceans. Furthermore, many rain gauge data only record the 6 hourly or even daily precipitation amounts (Villarini et al., 2008). Satellite passive microwave (PMW) sensors measure the thermal emission raindrops using their low frequency signals, and sense the scattering of upwelling radiation from the earth to space due to ice particles in the rain layer and tops of convective systems based on their higher frequency bands (Evans et al., 1995). However, PMW instruments can only be deployed on polar-orbiting satellite platforms (to date) due to the hardware technical challenges and they are too heavy to be carried by a geostationary satellites, which causes severe limitations for the spatiotemporal

resolutions of these PMW precipitation products unless the data are averaged substantially over time (Joyce et al., 2004).

With the advancements of AI and Big Data techniques, machine and deep learning methods have been developed to investigate climatological phenomena and predicted natural disasters (Yang et al., 2019). McGovern et al. (2017) applied Gradient Boosted Regression Trees (GBRT), RF, and elastic nets techniques using physical features of the environment (e.g. condensation level, humidity, updraft speed) to improve the predictability of high-impact weather events (e.g, storm duration, severe wind, severe hail, precipitation classification, forecasting for renewable energy, aviation turbulence). Cloud and precipitation properties are non-linearly related to the information extracted from meteorological data, including satellite images (Engström et al., 2015). Meyer et al. (2016) compared four machine learning (ML) algorithms (random forests (RF), neural networks (NNET), averaged neural networks (AVNNET), and support vector machines (SVM)) in precipitation area detection and precipitation rate assignment using SEVIRI data over Germany. They concluded that no single method was better than others, and modification in spectral parameters was of greater necessity than the choice of ML algorithms.

Although traditional machine learning methods have shown potential in precipitation detection and monitoring, deep learning (DL) approaches are more accurate in processing Big Data with various features (LeCun et al., 2015), most notably remote sensing images with better spatiotemporal resolution and more spectral information. To further examine the capability of deep neural networks (DNN), this paper proposes an

14

automatic rainy cloud detection system based on DNN models and compares the system

performance with that of traditional machine learning methods (e.g., SVM, RF). With the

high spatiotemporal resolution of ABI images, the proposed system has good

performance in real-time regional and local precipitation monitoring. Including full

coverage of precipitation characteristics of the study area, IMERG is a more accurate

assessment of precipitation attributes in contrast to discretely distributed ground

observations. This paper also evaluates the system in a hydrological extreme (e.g.,

hurricane) to provide a meaningful basis and reference for future studies.

**CHAPTER THREE HYPERSPECTRAL INFRARED SOUNDER CLOUD
FRACTION RETRIEVAL BASED ON DNN MODEL**

<u>Section One Introduction</u>

The objective of this research is to retrieve cloud fraction within each Cross-track

Infrared Sounder (CrIS) pixel based on deep learning method. The model used in this

study is deep neural network (DNN). Compared to traditional artificial neural networks

(ANN), it has multiple hidden layers which is suitable for large training data size with

various input predictors. The input predictors of the model proposed by this research are

derived from spectral information of CrIS observations. To reduce the number of

predictors thus improve the calculation efficiency, the study performs Principal

Component Analysis (PCA) and utilizes only the top 77 PCs as model predictors instead

of the original 2211 bands of CrIS data. The PC number is optimized by a series of

sensitivity tests, and the model parameters such as training iteration number, node

number and learning rate are also tuned and optimized by conducting the sensitivity tests.

The study seeks to contribute to the literatures on the cloud fraction retrieval topic in

the following aspects: 1. the study utilizes AI-based method to improve the operation

efficiency; 2. the study introduces PCA into the selection of model predictors to reduce

the predictor number but retain the full spectral information of CrIS data as well; 3. the

study introduce a method that uses the cloud mask of a higher-resolution sensor to decide

the cloud fractions of a lower-resolution hyperspectral sounder sensor. This method can

be used to the cloud retrieval of other similar sensor pairs.

Section Two Data

3.2.1 Cross-track Infrared Sounder

The CrIS is a Fourier transform spectrometer onboard the Suomi National Polar-

Orbiting Operational Environmental Satellite System (S-NPP) and Joint Polar Satellite

System (JPSS-1) satellites, which has significantly enhanced performance over NOAA's

legacy infrared sounder – the High Resolution Infrared Radiation Sounders (HIRS). The

CrIS spectrum is measured in three infrared regions by a 3×3 gridded detectors with a

nadir resolution of 13.5 km: long-wave from 650 to 1095 cm^{-1}, middle-wave from 1210

to 1750 cm^{-1}, and short-wave from 2155 to 2550 cm^{-1} (Han et al., 2013). The spectral

information of CrIS channels is shown in Figure 1.
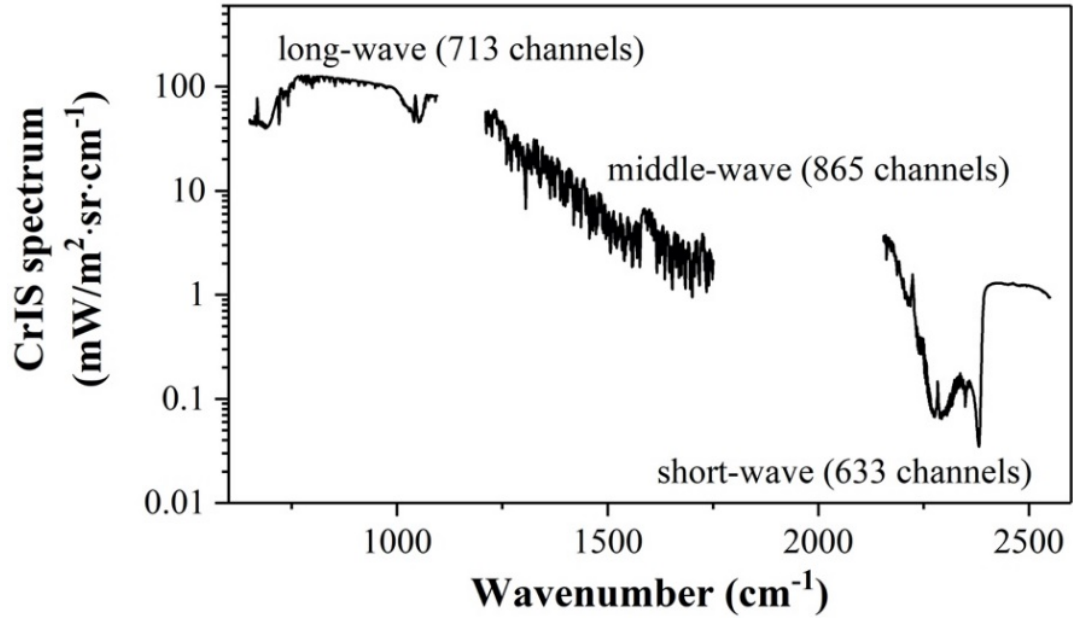
Figure 1. Spectral information of CrIS channels.

There are 34 field of regards (FOR) in one cross-track scanline, with 30 of them are Earth views, 2 of them are deep space views and the other 2 are instrument calibration views. In the normal spectral resolution (NSR) mode, the CrIS collects 1305 radiance channels with different spectral resolutions at the three infrared bands: 0.625 cm^{-1} in long-wave, 1.25 cm^{-1} in middle-wave, and 2.5 cm^{-1} in short-wave. The CrIS can also be operated in a full spectral resolution (FSR) mode. Under the FSR mode, the CrIS measures 2211 radiance channels over the three spectral regions with a spectral resolution of 0.625 cm^{-1} (Han and Chen, 2018). This study uses S-NPP CrIS FSR spectral information as the inputs and later performs a principal component (PC) transformation

on the original radiances to reduce the number of predictors and thus improve model efficiency.

3.2.2 Visible Infrared Imaging Radiometer Suite

The VIIRS, aboard the same platforms (S-NPP and JPSS-1) as CrIS, extends and improves upon a series of measurements initiated by certain legacy imagers, such as the AVHRR and MODIS. The VIIRS scans the earth spectrum in 22 radiance channels from visible ($0.412\ \mu$m) to the thermal infrared ($12.01\ \mu$m) bands (Cao et al., 2013), which includes 5 high spatial resolution bands (I-bands, 0.375 km at nadir), sixteen moderate spatial resolution bands (M-bands, 0.75 km at nadir), and one panchromatic day/night band (DNB, 0.75 km throughout the scan). In addition, it also provides various environmental products of the land, atmosphere, cryosphere, and ocean on a global scale with a higher spatial resolution and larger swath. As a key output from the VIIRS measurements, the VIIRS cloud mask (VCM) is now being widely used in different earth science studies. The VCM is determined by a series of strict checks (Kopp et al., 2014), with varying thresholds depending on different observational conditions. Its output has four flags, which are confidently clear, probably clear, probably cloudy, and confidently cloudy. The decimal values assigned to these four types are $0, 4, 8$ and 12, respectively. The VCM has a much finer spatial resolution than that of CrIS (0.75 km v.s 13.5 km), providing us with the opportunity to check CrIS's sub-pixel cloud coverage. In this study, the VCM is first collocated with CrIS FOV and then used to calculate the cloud fraction of CrIS which will be used as the learning target in the proposed model.

Section Three Method

This study introduces a new CrIS cloud fraction retrieval method based on the DNN model. Fundamentally, the CrIS sub-pixel cloud information is trained from VIIRS, which requires the CrIS and VIIRS measurements to be collocated together. Then, a series of hidden layers with different neurons is built and connected between the collocated CrIS spectra and VIIRS cloud mask for CrIS cloud fraction retrieval. After the proposed model is built, the cloud fraction is directly predicted at each FOV with all the CrIS channel radiances. Details of each step are summarized as follows.

3.3.1 Cloud fraction determination

The key to this study is to build the relationship between CrIS spectra and the cloud fraction determined by the VIIRS cloud mask, which needs the VIIRS cloud mask to be collocated with CrIS FOVs. The collocation is a time-consuming process, as it must search all the VIIRS pixels one-by-one at each CrIS FOV for accurate spatial and temporal collocation. Wang et al. (2016) developed an accurate collocation algorithm for CrIS and VIIRS based on their line-of-sight (LOS) pointing vectors at each CrIS FOV. Moreover, it uses a KD-tree searching strategy during the CrIS and VIIRS data pairing step, to reduces the collocation time. Previous research has confirmed that both CrIS and VIIRS are well-geolocation-calibrated instruments (Cao et al., 2013; Wang et al., 2013; Wang et al., 2017). Their collocation accuracy is at sub-pixel level with error less than 20 m (Wang et al., 2016). In this study, this collocation method is utilized to collocate CrIS spectra and the VIIRS cloud mask together.

After CrIS is collocated with VIIRS, the VIIRS pixels within CrIS FOV are then

adopted to calculate the cloud fraction of CrIS using equation (1),

$$CrIS_{(cf)} = \frac{N_{(Cloud,\ for\ VIIRS_{(VCM)} \geq 4)}}{N}$$ (1)

In equation (1), $CrIS_{(cf)}$ is the cloud fraction determined by the VIIRS cloud mask,

$N_{(Cloud)}$ and N are the number of VIIRS cloudy pixels and total number of VIIRS pixels

within CrIS FOV, respectively. Due to the geometric distortion caused by the scan

mirror rotation, the total number of VIIRS pixels N in each CrIS FOV is not a constant.

Instead, it changes with the scan mirror positions, ranging from around 200 to 1100 in

every CrIS scanline. For the total number of cloudy scenes $N_{(Cloud)}$ determination, only

confidently clear pixels are recognized as clear sky while the others are identified as

cloudy in this study. Since VIIRS has a much finer spatial resolution than CrIS (which

can be considered as a pure unit), the $CrIS_{(cf)}$ estimated from VIIRS provides accurate

subpixel cloud information for CrIS.

Figure 2 shows an example of the CrIS and VIIRS collocation and the cloud fraction

determination process. As shown in Figure 2a with the three VIIRS reflectance channels

composited true color image (R: 0.672 μm, G: 0.555 μm, B: 0.488 μm) as the

background, CrIS FOV footprint circled in orange is larger at the limb and smaller at the

nadir positions, which requires the geometric distortion effect to be precisely considered

during the collocation procedure. Figure 2b shows the specific nine CrIS FOVs at the 17th

FOR overlapping with the VIIRS true color image, and the corresponding collocated

VIIRS cloud mask as well as the CrIS cloud fraction determined by equation (1) are

presented in Figure 2c and 2d, respectively. As clearly shown, only a portion of clouds

enter into the above three CrIS FOVs, while the other six CrIS FOVs are completely

covered the clouds. With assistance from the collocated high spatial resolution VIIRS, the

CrIS cloud fraction information can be accurately estimated at every FOV. Figure 2e

shows the estimated cloud fraction for a whole CrIS scanline. As compared with Figure

2a, the estimated CrIS cloud fraction is generally consistent with the cloud distributions

shown in the VIIRS true color image.
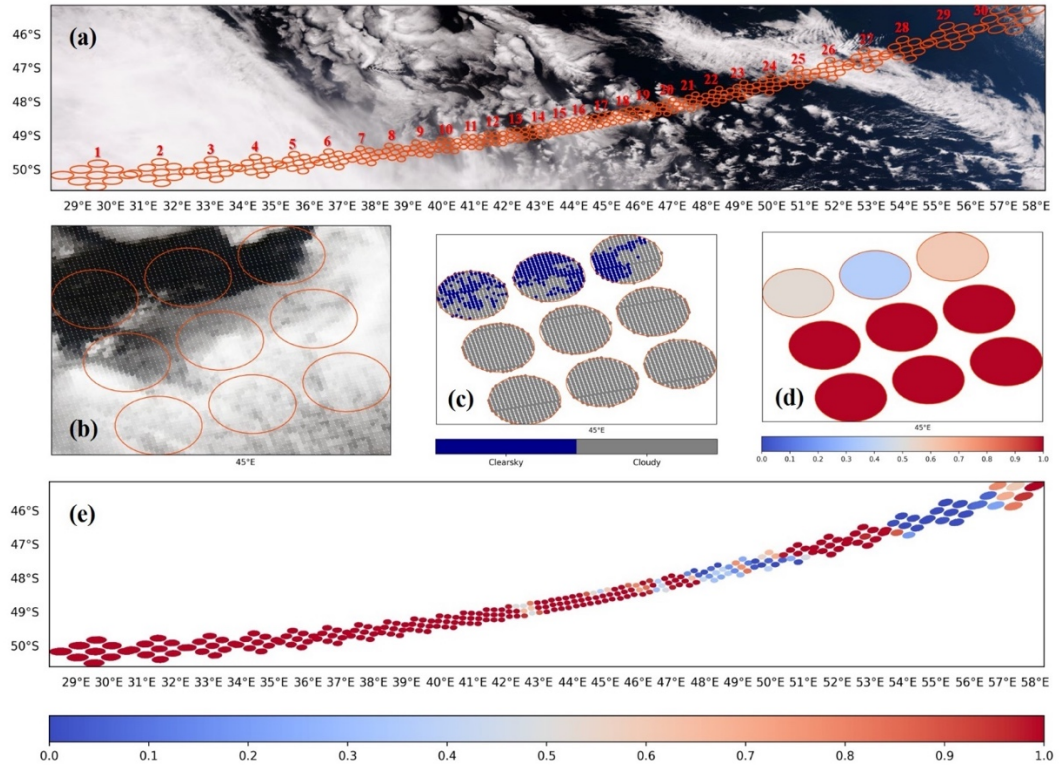
Figure 2. Example of the spatiotemporal data collocation between CrIS and VIIRS on Mar. 10, 2019: (a) The true color image of VIIRS overlapping with the footprints (orange circle) of CrIS in one selected cross-track scanline. Numbers in (a) represent the CrIS FOR position; (b) same as (a) but for the 17th CrIS FOR; (c) the collocated VIIRS cloud mask within 17th CrIS FOR; (d) the cloud fraction of CrIS calculated from VIIRS cloud mask at the 17th FOR with values ranging from 0 (clear sky) to 1 (completely cloudy); (e) same as (d) but for a whole CrIS scanline.

3.3.2 DNN model building

After the CrIS cloud fraction is determined, the next objective is to develop an accurate relationship between the CrIS spectra and the cloud fraction. To establish this connection, a data ensemble with sufficient samples is required. In order to include the general features and conditions of clouds, twelve days of the CrIS and VIIRS matched full orbit data pairs, covering every month (01/12, 02/07, 03/20, 04/03, 05/09, 06/27, 07/12, 08/16, 09/05, 10/22, 11/15, and 12/10) of 2018, are selected as the training dataset in this study. In addition to the training dataset, an optimized 5-layer neural network, including one input layer, one principal component (PC) transformation layer, three fully connected hidden layers, and one output layer, is built to train the CrIS spectra for cloud fraction estimation. The VIIRS determined CrIS cloud fraction is used as the learning target for the training as well as the accuracy evaluation.

23

For the input layer, all the CrIS FSR 2211 channel radiances are used as the predictors. As the radiances measured from hyperspectral infrared sounders are highly correlated, a de-correlation needs to be performed on the original CrIS spectra before sending them to the hidden layers for the purpose of better regression, convergence, and faster prediction. As such, a PC transformation layer is added between the input and hidden layers, and the CrIS channel radiances are then converted into the PC scores $CrIS_{pcs}$ through equation (2) (Xu et al., 2019),

$$CrIS_{pcs} = \left(CrIS_{spec} - \overline{CrIS_{spec}}\right) \times N^{-1} \times E^T \tag{2}$$

where $CrIS_{spec}$ is the CrIS measured spectral radiances, $\overline{CrIS_{spec}}$ is the mean radiances of the CrIS channels of the training dataset and N is the instrument noises. E are the eigenvectors decomposed from equation (3) with the training dataset:

$$S = E \times \Lambda \times E^T \tag{3}$$

where S is the covariance matrix of the noise normalized radiances and Λ is the diagonal eigenvalue matrix. The symbol $\times$ indicates matrix manipulation. By combining all the above matrices together, equation (2) finally becomes (4),

$$CrIS_{pcs} = CrIS_{spec} \times P_0 + W_0 \tag{4}$$

where P_0 is the PC transformation coefficients and W_0 is the channel dependent bias. The PC scores are a set of linearly uncorrelated new predictors that describe the same variances of the original dataset, and most of the effective Earth spectral variances are mainly distributed in the first few principal component scores. By only using the top k principal components as further predictors, one can greatly reduce the dimension and

noise of the original inputs. Sensitivity tests and discussion for the selection of $CrIS_{pcs}$ are conducted in Section 3.3.

The hidden layer using the PC scores as the inputs and further transform them into the intermediate results for the output layer using the learnable parameters (weights and biases). Three fully connected hidden layers with 64, 128, and 32 neurons in each layer respectively are used in the DNN model to yield the most accurate prediction. All of the three hidden layers are activated with the Rectified Linear Unit (ReLU) activation function for non-linear training,

$$ReLU(x) = \begin{cases} 0, for\ x < 0 \\ x, for\ x \geq 0 \end{cases} \tag{5}$$

where x in equation (5) is the input to a neuron. $ReLU$ is a very simple function that returns the value directly if it is positive and otherwise returns zero. This activation function is considered a significant milestone in the field of deep learning and is proven to be an efficient way to develop very deep neutral networks (Agostinelli et al., 2014). The neurons within the hidden layers are used to calculate the weights and biases to minimize the difference between the predictand and the truth value through forward and backward propagations during the training process. The output layer is also activated with a $ReLU$ function but was slightly modified, to correctly map the intermediate results produced by last hidden layers to the final cloud fraction with values ranging from 0 to 1. The modified $ReLU$ function $ReLU_{modified}$ is similar to the original but restricts the value to 1 if the input is higher than 1, because a cloud fraction output higher than 1.0 is physically unreasonable.

Finally, a total of 3,663,777 CrIS and VIIRS paired data samples are selected from 2018 and taken as training data, with a third randomly selected as the validation data to estimate model skill while tuning its hyperparameter. After the DNN model is successfully constructed, only the CrIS spectra is needed to estimate cloud fraction, avoiding the time intensive pre-processing steps and the data collocation. Equation (6) shows how the cloud fraction value is estimated by the DNN model using CrIS FSR spectra,

$$CrIS_{cf} = ReLU_{modified}(ReLU(ReLU(ReLU(CrIS_{spec} \times P_0 + W_0) \times P_1$$
$$+ W_1) \times P_2 + W_2)) \times P_3 + W_3) \times P_4 + W_4) \tag{6}$$

In equation (6), a CrIS spectrum $CrIS_{spec}$ is first converted to its $CrIS_{pcs}$ with P_0 and W_0. Then the $CrIS_{pcs}$ is further transformed to the intermediate results through three $ReLU$ activated hidden layers using the model trained coefficients P_1, P_2, P_3 and W_1, W_2, W_3. The outputs from last hidden layer are finally converted to the cloud fraction using P_4 and W_4 and the modified $ReLU$. All these model coefficients are determined by the training dataset during the training process. The proposed CrIS cloud fraction retrieval framework is illustrated in Figure 3.
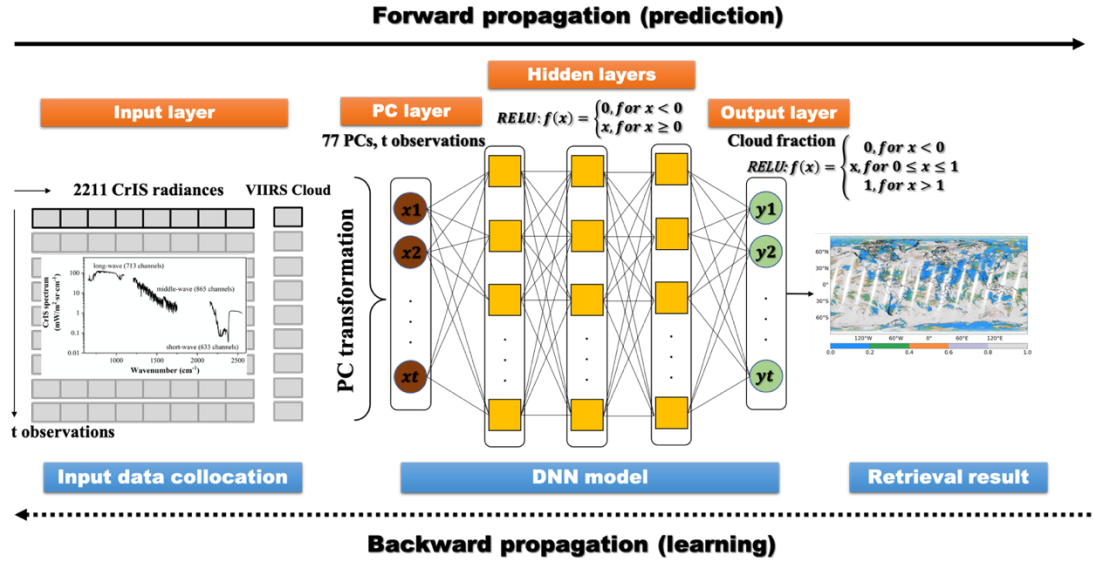
Figure 3. Flow chart of CrIS cloud fraction retrieval framework based on DNN model.

3.3.3 Model optimization

The adaptive moment estimation (Adam) and batch gradient descent (BGD) searching

strategy are adopted to optimize the loss function of the neural network during the model

training procedure. As mentioned in section 3.2, the PC scores of the raw CrIS spectral

data are firstly calculated before being entered into the hidden layers, in order to optimize

the model (e.g., de-correlation, dimensionality reduction, fast convergence and

predication). A two-step sensitivity analysis is performed to determine the optimized PC

predictors for the DNN model. Firstly, the model is trained and validated with different

numbers of PC predictors ranging in increments of 10 from 10 to 150. As the 10-step

sensitivity test line demonstrates in Figure 4, the best performing PC number producing the lowest mean square error (MSE), calculated from the differences of model predicted and the truth cloud fraction values of the training dataset based on one BGD iteration, falls between 60 and 90. After that, the model MSE shows a slightly increasing trend, which suggests that adding more PCs as model predictors would not improve the training accuracy. Based on the 10-step sensitivity test result, a further investigation is conducted by changing the PC numbers from 60 to 90 with a 1-step equal interval, to find the final PC predictors for the DNN model. Due to the stochastic characteristic of deep learning models, the optimized PC number with lowest MSE varies slightly in different set of training experiments even with the exact same parameters. Therefore, the sensitivity test repeats the second step 20 times (blue dish lines in the sub-plot of Figure 4) and uses their mean value (black solid lines in the sub-plot of Figure 4) to determine the best number of PC predictors. As the results show, a PC number of 77 produces the lowest MSE on average. Therefore, this study cuts off the CrIS principal component scores at 77 (red arrow line in the sub-plot of Figure 4), and only the top 77 $CrIS_{pcs}$ are used as the final predictors of the DNN model.
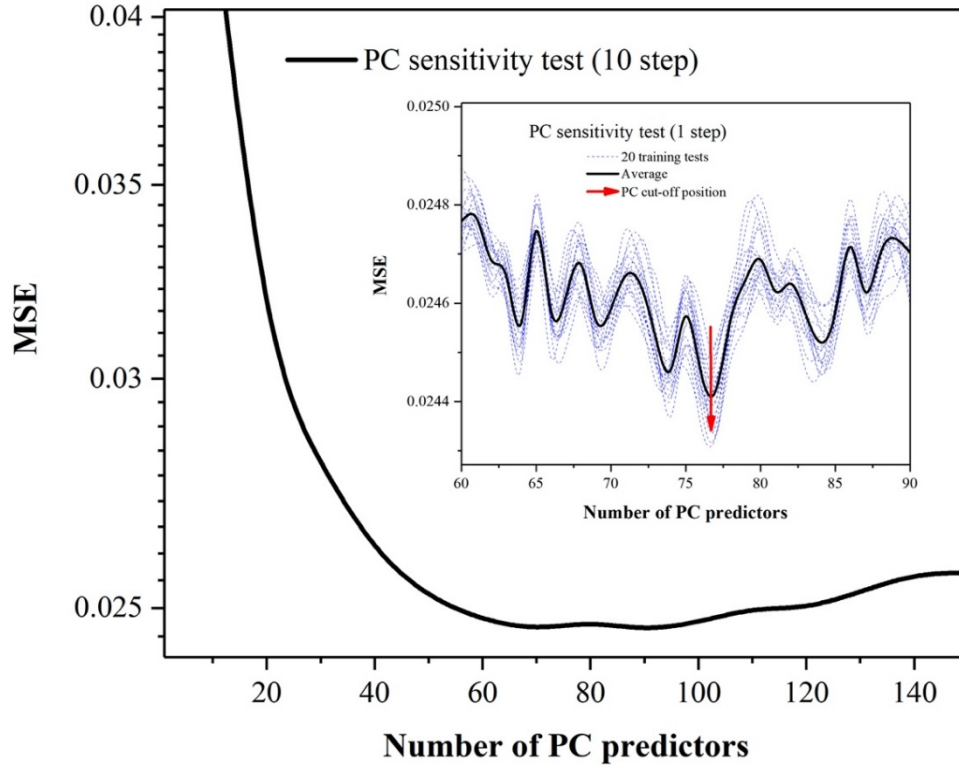
Figure 4. Sensitivity test result on the input PC number.

The DNN model is then trained with the selected PC predictors on a series of epochs until the MSE levels off, after the lowest point of MSE. To achieve this goal, this study adopts an adaptive learning rate strategy. Using 100 epochs as a training group, the model yielding the lowest MSE within the group is chosen. After one training group is finished, the model is further trained based on the best result (lowest MSE) of last training group, with an adjusted learning rate decayed by half of the previous one. The training procedure is finally terminated when the MSE of the validation plateaus. The choice of

the starting learning rate is arbitrary. In this study, it is set as 0.001 at the beginning.

Figure 5 shows the lowest model MSE as a function of the training group on the training

data (red line) and validation (blue line) data separately. As clearly shown, the training

MSE keeps decreasing as more training is conducted. However, the validation MSE stays

relatively consistent after 6th training group. This suggests that the model may have

learned the training dataset after the 6th training group, and additional training has no

significant improvement upon the validation dataset. It is therefore unnecessary to

conduct more training after this point. In addition, it is reasonable to see a lower

validation MSE as compared with the training result, since the model uses a dropout

regularization (the neuron dropout rate is 5%) at each hidden layer to avoid potential

over-fitting. The dropout is only activated during the training phase but deactivated when

evaluating on the validation data, resulting in a better function in the latter case. Finally,

the model is determined at the 60th epoch of the 8th training group which yields the lowest

validation MSE of 0.0152 among all of the total 800 training epochs.
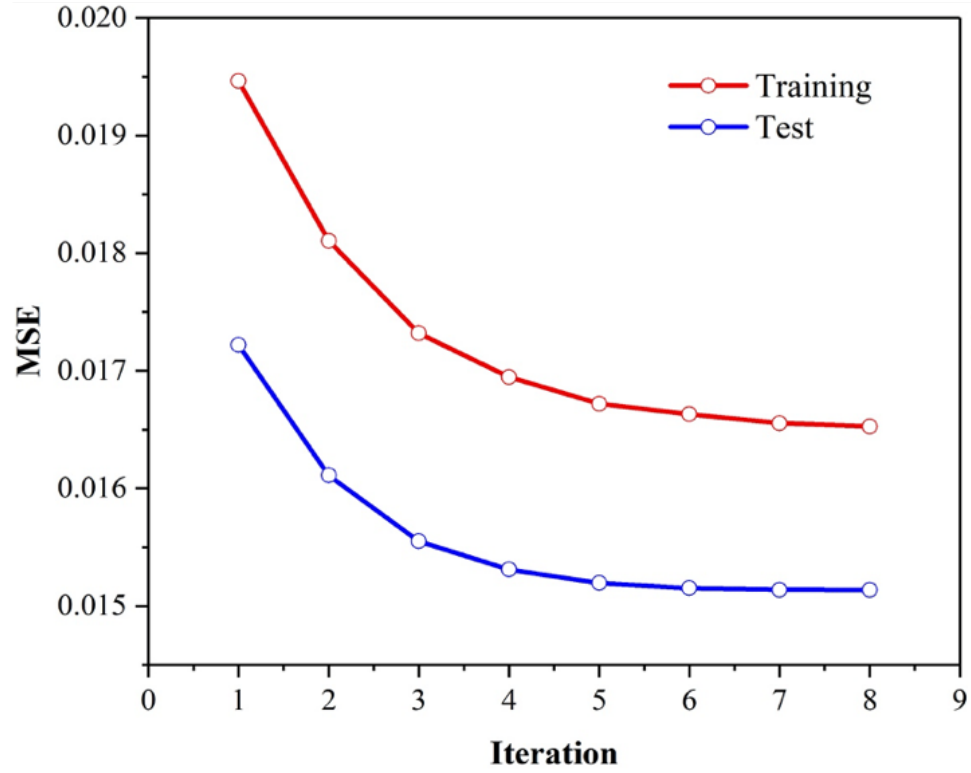
Figure 5. The lowest model MSE per training group on the training and validation datasets.

3.3.4 Model accuracy analysis

The accuracy of the proposed DNN model is analyzed based on a test (or holdout) dataset with 1,242,720 data samples in total selected from four different seasons of Feb. 15, May 15, Jul. 10 and Nov. 10 of 2018. The test data for this accuracy analysis is different from the validation data mentioned in previous sections. It is an independent dataset which has not been used during the model training, and it can thus produce an

unbiased estimate of final DNN model's performance. In addition to the MSE discussed at the training stage, the Pearson's correlation coefficient (R) is also adopted as a metric to evaluate the model accuracy by measuring the correlation between the model prediction and truth.

As shown in Figure 6, the predicted CrIS cloud fraction is mostly distributed near the 1:1 diagonal line (black dish line) with high probability density. The fitting line (solid red line) with a slope of 1.002 and very tiny bias of 0.007, nearly overlaps the diagonal line, indicating a very solid correlation between the model prediction and truth. Additionally, the reliable performance of the DNN model can be illustrated due its low MSE of 0.021 and high R value of 0.924. As compared with Figure 6, the MSE calculated from the test data is only slightly higher than that calculated from both the training and validation data during the training process, indicating that the model is well trained with neither significant under-fitting nor over-fitting.
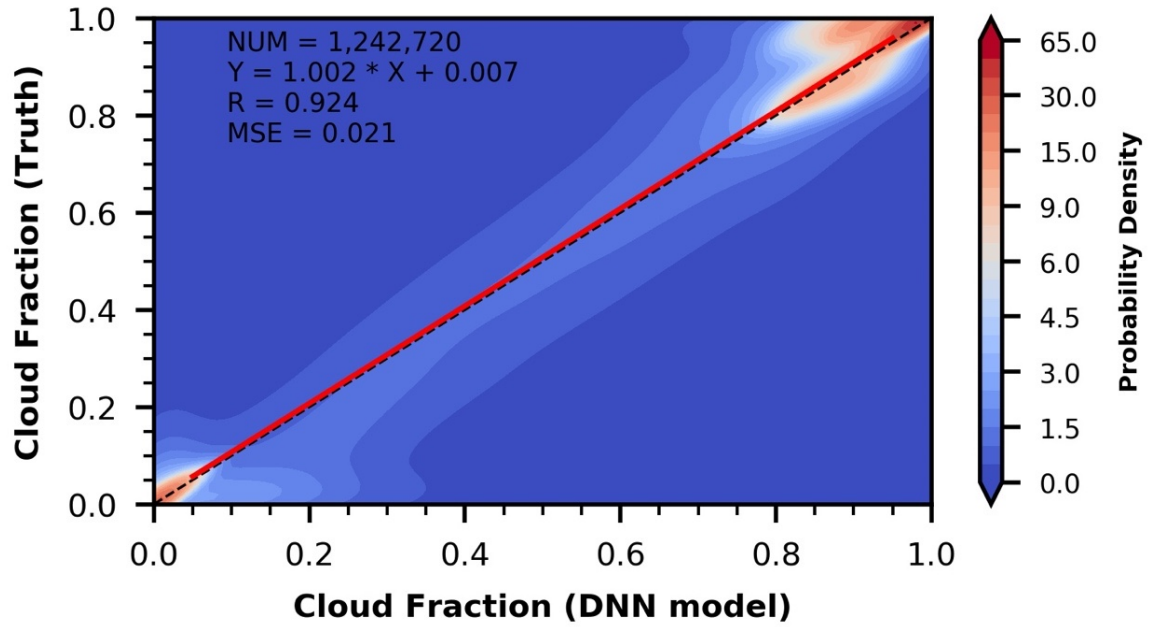
Figure 6. Probability density plot of the DNN model predicted and truth cloud fractions. The red solid line and black dish line are the fitting line and 1:1 diagonal line, respectively.

Figure 7 shows the differences between DNN predicted cloud fraction and the truth cloud fraction. The blue dot and vertical error bar represent the mean and standard deviation of their differences in the corresponding bins (the bin size is 0.05), respectively. As shown, the 1-sigma uncertainty at each bin is not identical, ranging from 0.108 to 0.182. The uncertainty in the low cloud fraction regions (partially thin cloudy scenes) is overall slightly higher than that in the high cloud fraction, where the scenes are almost

fully covered by clouds. This is because the spectral features of thin cloud and clear sky are very similar to each other. Moreover, the mixed strong surface signals can increase the complexity of the spectra observed in the thin partially cloudy scenes, which may result in a higher retrieval uncertainty in these areas. Another point that can be identified from Figure 7 is that the DNN model tends to overestimate the cloud fraction with values less than 0.5, especially for those very thin partially cloudy scenes. The average overestimation is around 0.078 for cloud fraction less than 0.1. On the other hand, cloud fraction with values over 0.5 are likely to be underestimated. The largest negative difference between model predictions and the truth values are located near 1.0 with an average underestimation of 0.085. The main explanation for this is that the relationship between CrIS spectra and the cloud fraction is nonlinear, which results in the predictions from the DNN model to systematically overestimate the actual values for one range and underestimate them for another. We should also be aware that cutting off PCs may potentially reduce the model accuracy, because the abandoned PCs may also contain some cloud fraction related information. However, considering the effectiveness of PCA on reducing the data complexity of hyperspectral infrared sounders, conducting PC transformation is worthwhile as it indeed optimizes the model inputs. Nevertheless, the predictions overall agree well with the considered truth values with a high correlation coefficient of 0.924, as shown in Figure 5.
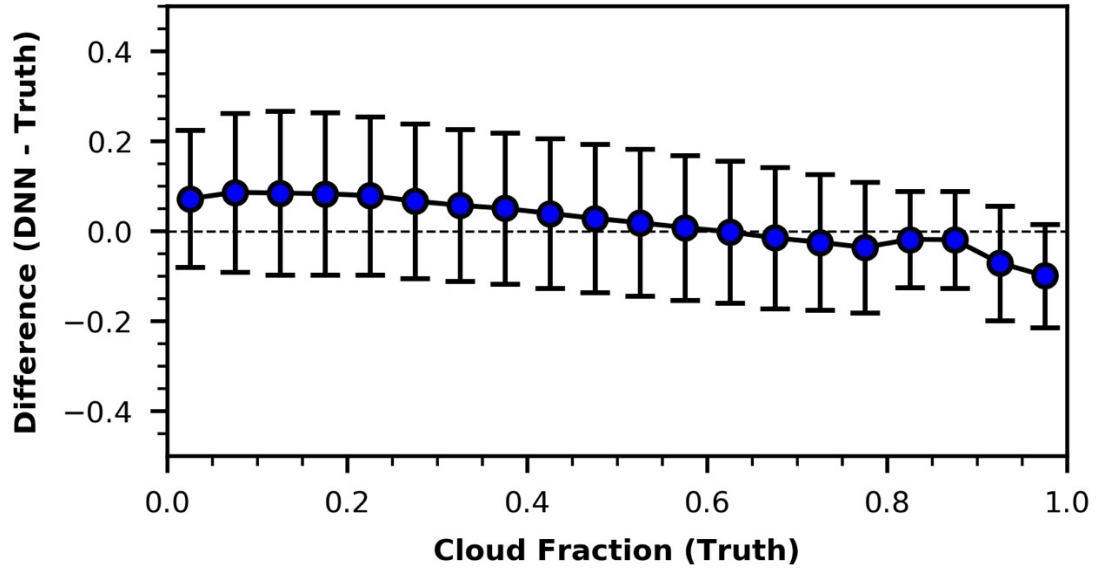
Figure 7. Distribution of difference between predicted and truth cloud fractions as a function of cloud fraction. Blue dot and error bar indicates the mean bias and standard deviation of the difference in the corresponding interval (0.05), respectively.

Section Four Use Case Study

The performance of the proposed cloud fraction retrieval model is investigated on a series of independent use cases selected from 2018 and 2019, all of which are excluded from the training dataset to prevent bias in error estimates.

3.4.1 Oct. 30, 2018

Figure 8 shows the daytime global cloud distribution maps of Oct. 30, 2018. As presented in the VIIRS true color image (Figure 8a), more than 60% of the global land

and ocean areas are covered by clouds. This can also be identified in Figure 8b, the truth

CrIS cloud fraction map, that was determined by the VIIRS cloud mask. The purely clear

sky and partially thin cloudy scenes (blue areas with cloud fraction less than 0.2) are

mainly located over the land part of the coastal areas of United States, southern Argentina,

Sahara Desert, southern Africa, southwest Asia, north India, northwest China, and large

portions of Australia and Antarctica. Given the retrieval results produced by the proposed

DNN model (shown in Figure 8c) compared to that of Figure 8b, the DNN model

accurately predicts the majority of the cloud fraction. Their difference map shown in

Figure 8d further confirms that the cloud fraction retrieved from the DNN model agree

well with the truth values on a global scale. Moreover, their residuals are almost

uniformly distributed around the zero line, with a mean of -0.007 and standard deviation

of 0.134, and most of them are less than 0.2 (~91%) and 0.1 (~74%), as evidently shown

in Figure 8e. However, relatively larger difference values are observed over the partially

thin cloudy areas, especially over high latitude areas (Figure 8d). As mentioned, this is

possibly due to the strong surface signals, which makes it hard for the model to correctly

classify thin clouds. This may also be attributed to the relatively low accuracy of cloud

mask product of VIIRS (which is adopted as the learning target) over high latitude areas,

which are ~88% in snow covered land and 72% in Antarctic and Greenland (Zhou et al,

2019). The inaccurate inputs from VIIRS in these scenarios will introduce inaccuracy to

the model during training, thus reducing the model's ability to correctly estimate cloud

fraction over these areas. In addition, both VIIRS and CrIS have larger instrument noises

over the cold scenes, which may also reduce the accuracy over the high latitude regions.

Figure 8f illustrates the quantitative relationship between the model predictions and truth. A favorable correlation of 0.929 between the CrIS predicted and VIIRS determined cloud fraction is obtained for this particular case. The daytime MSE is 0.018, which is slightly lower than that of the model value as discussed in section 3.4. All these statistics demonstrate that the proposed DNN model works very well for the daytime cloud fraction retrievals.
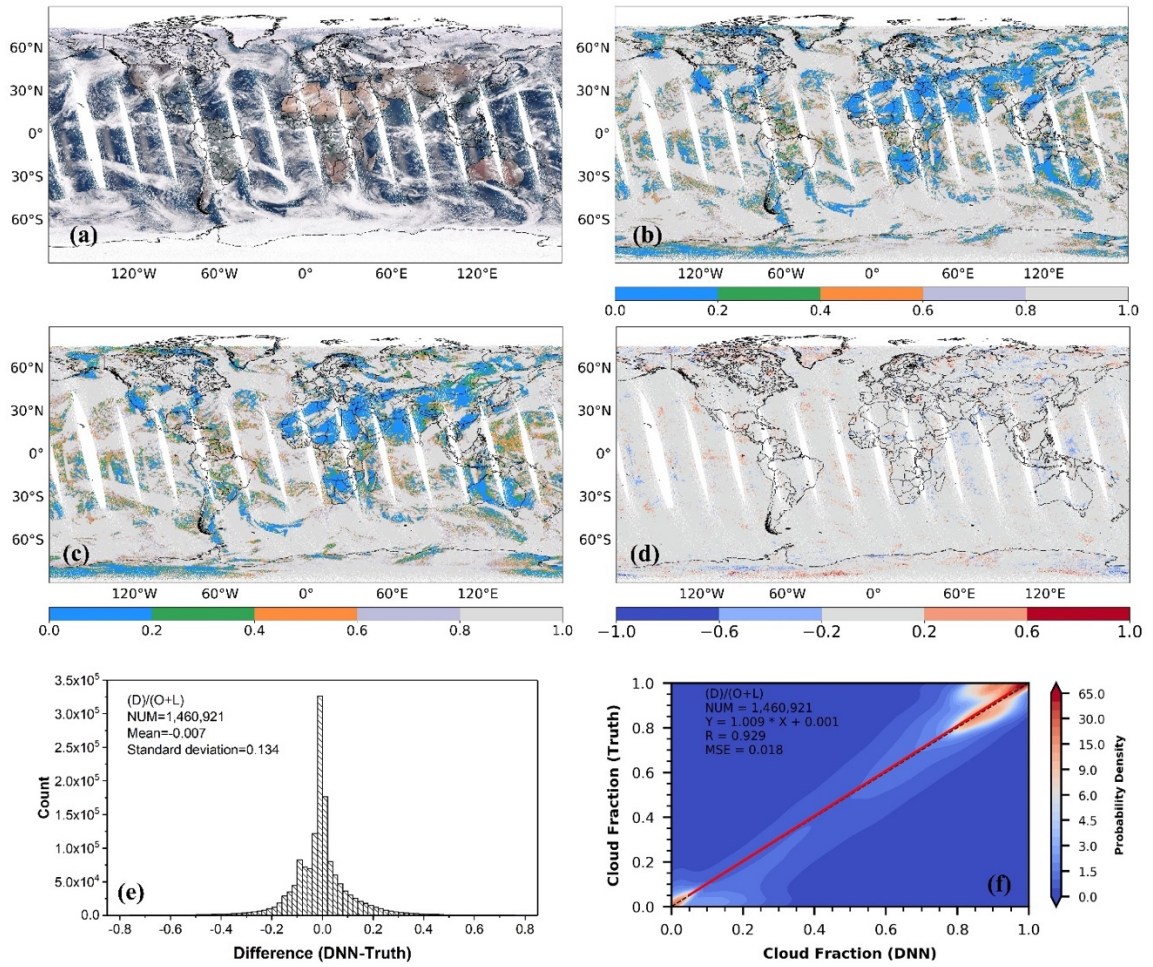
Figure 8. Daytime of Oct. 30, 2018. (a) The VIIRS true color imagery; (b) Truth CrIS cloud fraction calculated using VIIRS cloud mask; (c) CrIS cloud fraction predicted by the proposed model; (d) Difference between (c) and (b); (e) the histogram of (d); (f)

Probability density plot of the model prediction and truth. The "D/O+L" in (e) and (f) represents all of the daytime (D) ocean (O) and land (L) data. The red solid line and black dish line in (f) are the fitting line and 1:1 diagonal line.

The investigation on the model nighttime performance is also conducted in this study, and the results are presented in Figure 9. Since the reflectance channels are not available at night, the VIIRS moderate resolution band 14 (M14 at 8.55 μm) brightness temperature is used as the reference image (Figure 9a) for this discussion. Essentially, the lower the brightness temperature, the more likely the scene is contaminated by clouds, especially over low latitude regions, such as those in tropical areas which might be covered by deep convective clouds. As indicated by the truth CrIS cloud fraction in Figure 9b and compared with the model prediction in Figure 9c, it is encouraging to see that the results retrieved from the DNN model are consistent with the truth values over nighttime observations. Similar to the daytime case, their larger differences are mainly observed over the poles and other snow-covered regions (as shown in Figure 9d), partially due to the relatively poor performance of VIIRS cloud mask. The statistical result in Figure 9e show a tiny negative bias of -0.013, suggesting that the nighttime retrieval result is slightly underestimated. This can also be identified from the positive offset of the fitting line (solid red line) shown in Figure 9f. The standard deviation is 0.151 also implies that the overall uncertainty of the nighttime retrieval results is slightly

higher than that of the daytime (0.134). Regardless, the metrics shown in Figure 9f still

suggest a high similarity between the model predictions and truth. According to the

colored probability density plot, the fitting line is nearly coincident with the 1:1 line,

revealing a relatively accurate estimation from the DNN model as compared with truth.

The low MSE (0.023) and high R (0.914) further confirms that the model is performs

very well for nighttime observations.
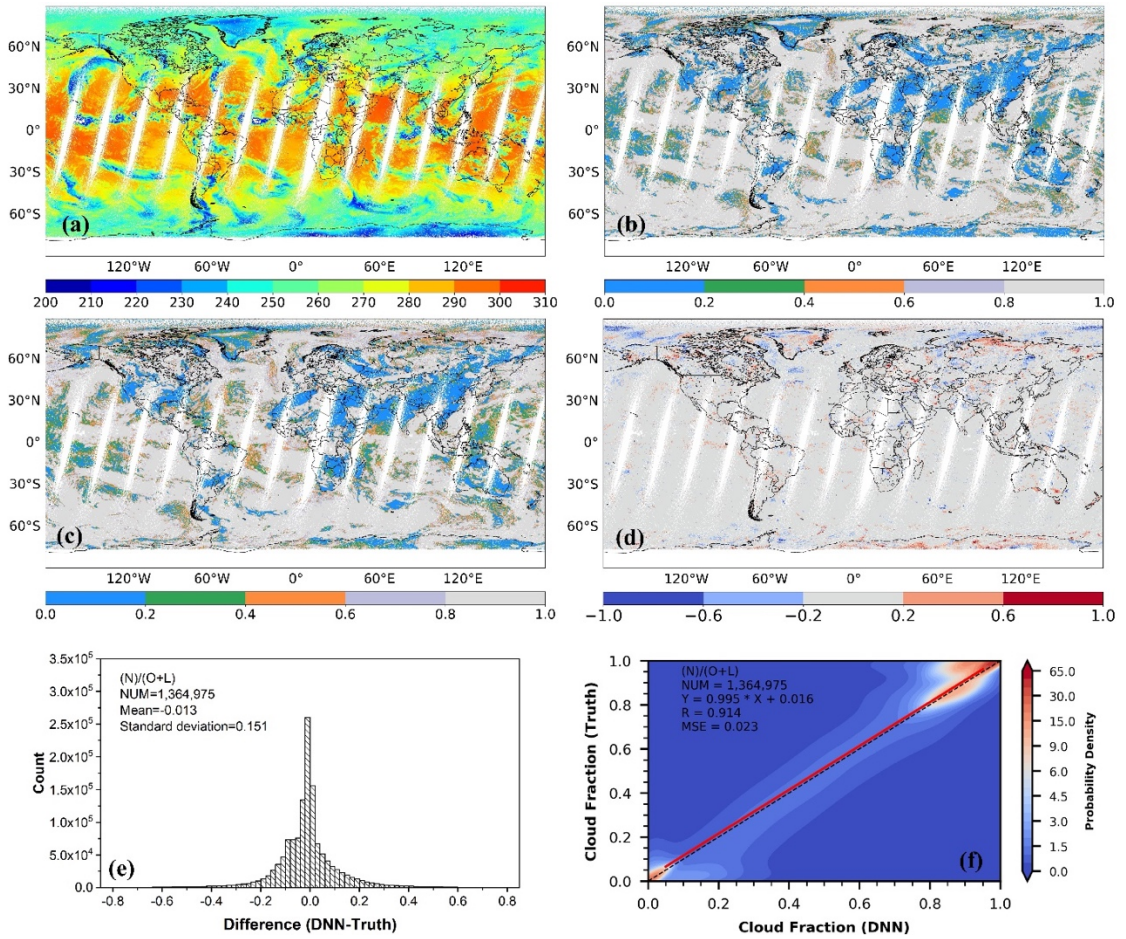
Figure 9. same as Figure 8 but for the nighttime of Oct. 30, 2018. Particularly, the VIIRS

M14 brightness temperature is used as the reference image in (a) instead of the true color

image, as the reflectance channels are not available at night. The "N/O+L" in (e) and (f) represents all of the nighttime (N) ocean (O) and land (L) data.

Table 1 presents detailed quantitative comparisons between results calculated from the daytime and nighttime data. In general, the DNN model achieves a higher accuracy over daytime than nighttime, with a lower MSE (0.018 vs 0.023) and higher R (0.929 vs 0.914). The lower accuracy observed in the nighttime case is likely due to the weaker signal received by CrIS at nighttime, which makes the spectral contrast among FOVs much smaller. A similar mechanism can occur in the VIIRS instrument, leading to a relatively lower accuracy of the nighttime cloud mask as well as truth cloud fraction. Furthermore, the model tends to exhibit better performance over the ocean than the land areas. The averaged (day and night) MSE and correlation coefficient over ocean are 0.015 and 0.930, respectively, while over land they are 0.032 and 0.902, respectively. The main explanation for this is that the surface cover over land is more heterogenous than that of ocean, which increases the complexity of the satellite observed spectra over land. In addition, the mixed-pixel issue (inhomogeneous scene) over land also increases the difficulty of accurate cloud identification.

Table 1. Test metrics of the model accuracy on Oct. 30, 2018.

Date	Metrics	Daytime			Nighttime			Total
		Land	Ocean	Globe	Land	Ocean	Globe	

10/30	MSE	0.029	0.011	0.018	0.035	0.018	0.023	0.020
/2018	R	0.908	0.944	0.929	0.896	0.916	0.914	0.922

3.4.2 Jun. 1 to Jun. 7, 2020

One week of the global CrIS and VIIRS data selected from Jun 1 to Jun. 7, 2020, are further analyzed in the following study, to evaluate the robust performance of the DNN model, with results summarized in Table 2.

The accuracy metrics shown in Table 1 demonstrate that the proposed cloud fraction retrieval model produces reliable and robust predictions for a continuous seven days. For the daytime, the model MSE has little fluctuation, with values ranging from 0.015 to 0.018 over land, and from 0.012 to 0.014 over ocean in this one-week analysis. The cloud fraction correlation coefficient between DNN model predictions and the truth values is relatively high and stable for all the daytime cases, averaging 0.944. The model MSE at nighttime has a slightly larger variation than the daytime MSE, fluctuating between 0.040 to 0.053 over land, and between 0.019 and 0.023 over ocean. The mean correlation coefficient at nighttime is 0.904 with values ranging from 0.889 to 0.913. On the whole, the global (all ocean, land, daytime, and nighttime) mean MSE and correlation coefficient are 0.021 and 0.922 respectively for these selected continuous use cases, which are comparable to the model metrics (0.021 and 0.924) as discussed in the previous section.

All tests demonstrate the stability of the DNN model and illustrate its potential to be an effective tool for cloud fraction retrieval.

Table 2. Test metrics of the model accuracy from Jun. 01 2020 to Jun. 07 2020.

Date	Metrics	Daytime			Nighttime			Total
		Land	Ocean	Globe	Land	Ocean	Globe	
06/01	MSE	0.015	0.014	0.014	0.044	0.023	0.030	0.022
/2020	R	0.951	0.934	0.944	0.875	0.902	0.897	0.920
06/02	MSE	0.016	0.014	0.014	0.052	0.022	0.033	0.023
/2020	R	0.949	0.930	0.942	0.842	0.905	0.889	0.915
06/03	MSE	0.017	0.013	0.014	0.048	0.019	0.029	0.021
/2020	R	0.944	0.935	0.943	0.854	0.918	0.902	0.923
06/04	MSE	0.017	0.012	0.014	0.04	0.019	0.025	0.019
/2020	R	0.943	0.937	0.944	0.881	0.921	0.913	0.929
06/05	MSE	0.018	0.013	0.014	0.050	0.019	0.029	0.021
/2020	R	0.943	0.938	0.945	0.851	0.921	0.900	0.922
06/06	MSE	0.016	0.013	0.014	0.048	0.019	0.029	0.021
/2020	R	0.950	0.937	0.946	0.861	0.921	0.903	0.924
06/07	MSE	0.017	0.013	0.014	0.053	0.019	0.030	0.022
/2020	R	0.947	0.937	0.945	0.844	0.924	0.900	0.922
Mean	MSE	0.017	0.013	0.014	0.048	0.020	0.030	0.021

CHAPTER FOUR RAINY CLOUD CLASSIFICATION

Section One Introduction

This research proposes an automatic rainy cloud detection system based on DNN models and compares the system's performance with that of traditional machine learning methods (e.g., SVM, RF). The new Advanced Baseline Imager (ABI) onboard the GOES-16 satellite is adopted to classify rainy and non-rainy clouds based on the brightness temperature differences (BTDs) and reflectances (Ref) derived from ABI. Convective and stratiform rain clouds are also separated using similar spectral parameters expressing the characteristics of cloud properties. The precipitation events used for training and validation are obtained from the IMERG V05B data, covering the southeastern coast of the U.S. during the 2018 rainy season.

With the high spatiotemporal resolution of ABI images, the proposed system has good performance in real-time regional and local precipitation monitoring. Including full coverage of precipitation characteristics of the study area, IMERG is a more accurate assessment of precipitation attributes in contrast to discretely distributed ground observations. This paper also evaluates the system in a hydrological extreme (e.g., hurricane) to provide a meaningful basis and reference for future studies.

Section Two Data and Spectral Parameters

4.2.1. Study area

  The study focuses on a rectangular area of the U.S. east coast (32°N to 39°N, 80°W to 75°W) crossing Pennsylvania, Delaware, Maryland, Washington DC, Virginia, and North and South Carolina (Figure 10). The study area's climate is characterized by cool to cold winters and hot, humid summers. Precipitation volume, frequency, and density are significantly higher in all seasons than in other parts of the U.S. (Liu et al., 2017). A plethora of training and testing samples for both stratiform and convective precipitation are extractable to build the classification models and making the area suitable for the study of precipitation. A large number of hurricanes and tropical cyclones made landfall in this area in the past 100 years, making the rainy cloud classification system practical on hydrological disasters such as hurricanes.
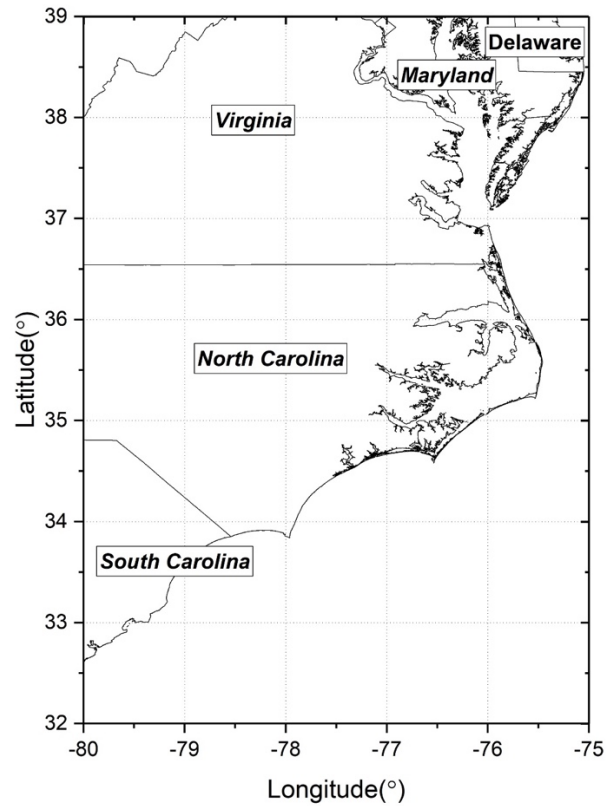
Figure 10. Geographic coverage of study area

4.2.2. GPM-IMERG precipitation estimates

Instead of rain gauge data that are commonly used in precipitation detection

research, Integrated Multi-satellite Retrievals for the GPM (IMERG) V5B precipitation

product is used in this research to distinguish rainy/non-rainy areas and

convective/stratiform areas. The IMERG has a spatiotemporal resolution of 0.1° and 30-

minutes, respectively. The precipitation product is generated based on five steps: 1) retrieval algorithm produces and inter-calibrates the Passive Microwave (PMW) estimates; 2) spatiotemporal interpolations are carried out to obtain adequate sampling; 3) holes are filled in PMW constellation using microwave-calibrated IR estimates; 4) gauge observations are adopted to control bias; and 5) error estimates and product delivery are accomplished (Huffman et al, 2018). The IMERG is a series of state-of-the-art high-resolution QPE (Quantitative Precipitation Estimation) products, higher in spatial and temporal resolutions, and lower in bias with ground truth compared to the former TRMM series. It is a merged dataset that makes full use of various global scale PMW and IR constellations and is one of the most accurate and popular precipitation products (Rios et a., 2017; Wei et al., 2018). It has relatively high accuracy in deciding the rainy areas and convective areas.

Gauge data are not used in this study for the following reasons: 1) Gauge observations are distributed sparsely in our study area with the density of 0.035 gauge per 100 km^2 (122 gauges in the study area of 350,000 km^2), and the sparseness of this distribution does not provide enough training and testing samples for the models and is insufficient in reflecting sky conditions; 2) publicly-accessible gauge observations are usually non-uniform in temporal resolution resulting in the samples being distributed unevenly in a different time and introducing bias to the models. For example, some of the gauge records are at an hourly time step, while others have a time step of 30 or 15 minutes; this feature might not capture short-temporal convective precipitation events.

4.2.3. GOES-16 ABI data

The Geostationary Operational Environmental Satellite (GOES)-16 is the current operational geostationary satellite operated by National Oceanic and Atmospheric Administration (NOAA) and National Aeronautics and Space Administration (NASA) and is also known as GOES-East member of the GOES-West and GOES-East NOAA system. It was launched on November 9, 2016, and has provided data since November 2017. The Advanced Baseline Imager (ABI) instrument onboard GOES-16 provides 16 spectral bands, including two VIS, four near-infrared (NIR), and ten IR channels. Due to the lack of the three VIS and NIR bands during nighttime, this research focuses on the rainy cloud detection and convective area delineation in the daytime. Eleven bands are used to calculate the spectral parameters in the detection and delineation procedure (i.e., 2, 3, 6, 8, 10, 11, 12, 13, 14, 15,16). Detailed information regarding the central wavelengths and spatial resolutions for each band are available in **Table 3** (Benz et al., 2018). The ABI generates an image of the Contiguous U.S. (CONUS) every five minutes, and its L1b data used in the study are accurately registered (resampled) to a fixed grid (angle-angle coordinate system) with three different spatial resolutions at nadir (GOES-R Series Program Office, 2019) ranging from 0.5 to 1 km and 2 km for different bands. Since it has different spatial and temporal resolutions from that of IMERG, collocating the ABI and IMERG data in both space and time dimensions is needed (Section 3.1).

Table 3. ABI Band Characteristics

Band Number	Central Wavelength (μm)	Spatial Resolution at nadir (km)	κ-factor (W^{-1}*m *μm)	Used in study	Primary Application
1	0.47	1.0	1.5177^{-3}		Aerosols
2	0.64	0.5	1.8767^{-3}	√	Clouds
3	0.865	1.0	3.1988^{-3}	√	Vegetation
4	1.378	2.0	8.4828^{-3}		Cirrus
5	1.61	1.0	1.26225^{-2}		Snow/ice discrimination, cloud phase
6	2.24	2.0	3.98109^{-2}	√	Cloud particle size, snow cloud phase
7	3.9	2.0	-		Fog, stratus, fire, volcanism
8	6.19	2.0	-	√	Various atmospheric features
9	6.95	2.0	-		Middle-level water vapor features
10	7.34	2.0	-	√	Lower-level water vapor features

11	8.5	2.0	-	√	Cloud-top phase
12	9.61	2.0	-	√	Total column of ozone
13	10.35	2.0	-	√	Clouds
14	11.2	2.0	-	√	Clouds
15	12.3	2.0	-	√	Clouds
16	13.3	2.0	-	√	Air temperature, clouds

4.2.4. Spectral parameters

The ability of a particular kind of cloud to produce precipitation and develop heavy rate convective precipitation depends on the altitude of the cloud top and the thickness of the cloud (Cotton et al., 2010). If a cloud is high enough in altitude, thick enough to carry a large volume of water vapor, and contains ice particles in its upper cloud layers, the chance of producing precipitation increases. The measurement of the vertically-integrated liquid water content in clouds is expressed as the Liquid Water Path (LWP) as shown in Equation (7), an effective measurement of the potential for precipitation to form in the clouds (Reid et al., 1999; Chen et al., 2018; Han et al., 1994; Nakajima et al., 1995):

$$\text{LWP} = \frac{5}{9}\rho_w \tau r_e(h) \tag{7}$$

where ρ_w (g/m^3) is the density of liquid water, τ is the optical thickness, and $r_e(h)$ is the cloud effective radius determined by the cloud thickness (h). The 2.24 μm channel

49

reflects cloud particle size, especially for those below the cloud top (Lindstrom et al.,

2017); therefore, it reflects the LWP and thereby provides useful information in rainy

cloud identification.

To classify different types of sky conditions and clouds according to the precipitation properties, the LWP is reflected by the spectral parameters. Cloud top temperature (CTT) is a direct indicator of parameters in LWP and reflecting cloud altitude. The CTT is related to the intensity of precipitation with colder cloud tops being more likely to produce heavier precipitation (Vijaykumar et al., 2017). The IR channels of ABI provide CTT information in different spectral ranges. The VIS and NIR bands reflect the unique color and brightness of rainy clouds in the daytime (Scofield, 1987). Effective spectral parameters of the classification system are created and calculated from the combinations of these bands from VIS to far IR. Due to the lack of VIS and NIR information in the nighttime, this research focuses on daytime rain cloud monitoring. In total 15 spectral parameters are selected to optimize the detection accuracy and include $BT_{10.35}$, $\Delta BT_{6.19-10.35}$, $\Delta BT_{7.34-12.3}$, $\Delta BT_{6.19-7.34}$, $\Delta BT_{13.3-10.35}$, $\Delta BT_{9.61-13.3}$, $\Delta BT_{8.5-10.35}$, $\Delta BT_{8.5-12.3}$, $BT_{6.19}$, $\Delta BT_{7.34-8.5}$, $\Delta BT_{7.34-11.2}$, $\Delta BT_{11.2-12.3}$, and Reflectance (Ref) of 3 VIS and NIR bands, $Ref_{0.64}$, $Ref_{0.865}$ and $Ref_{2.24}$. For BT and Ref, the subscript number is the central wavelength of the band, and for BTD (ΔBT) the subscript numbers indicate the central wavelengths (

Table 4).

Table 4. Spectral parameters used in the models, with the subscript number

being the central wavelength (μm).

Spectral parameters	Cloud Features reflected by the parameter
Ref0.64	Cloud brightness
Ref0.865	Cloud brightness
Ref2.24	Cloud particle size
BT10.35	Cloud particle size, cloud top temperature
△BT6.19-10.35	Cloud top temperature, convective level
△BT7.34-12.3	Cloud top temperature, convective level
△BT6.19-7.34	Cloud height and thickness
△BT13.3-10.35	Cloud top height
△BT9.61-13.3	Cloud top height
△BT8.5-10.35	Cloud phase (positive for thick ice clouds, negative for thin low-level water clouds)
△BT8.5-12.3	Optical thickness (negative values for thin optical thickness)
BT6.19	Upper-level tropospheric water vapor
△BT7.34-8.5	Cloud optical thickness
△BT7.34-11.2	Cloud top temperature and height
△BT11.2-12.3	Cloud thickness, particle size

The 10.35μm channel is an atmospheric window channel providing the rich CTT information. It is effective in precipitation estimation and especially for convective areas (Giannakos and Feidas, 2013). The low temperature in this band indicates a high cloud with a higher probability of producing precipitation and developing into a convective event. The 13.3 μm is the CO_2 absorption channel, and CO_2 decreases with altitude. Therefore, this channel's temperature is smaller for lower-level versus higher-level clouds. Since the temperature in 10.35 μm has an inverse relationship with height, $\Delta BT_{13.3\text{-}10.35}$ is useful in estimating cloud top height.

The 6.19 μm and 7.34 μm are water vapor channels; the differences between their brightness temperatures and those observed in the longwave IR bands (i.e., 10.35μm,12.3μm) represent the summit altitude of the cloud. These BTDs are accurate indicators about whether the cloud level is high enough to become convective areas. At low altitudes, cloud temperature in water vapor channels is lower than that in 10.35 and 12.3 μm bands due to the water vapor absorption. As a result, $\Delta BT_{6.19\text{-}10.35}$ and $BT_{7.34\text{-}12.3}$ return negative values for low clouds and slightly negative values for rainy clouds, especially convective clouds. The $\Delta BT_{6.19\text{-}7.34}$ is also adopted because it reflects cloud height and thickness with significantly negative values for mid-level clouds and small negative values for the high thick clouds (Feidas and Giannakos, 2012). Additionally, the BT of the upper-level water vapor channel (6.19 μm) is an independent parameter due to its capability to detect rainy and convective clouds.

The information derived from the 11.2 μm channel is similar to that of 10.35 μm channel, so $\Delta BT_{7.34\text{-}11.2}$ reflects the CTT and cloud height. The BTD between 10.35 and 12.3 μm is effective in estimating low-level moisture and cloud particle size (Schmit et al., 2017).

The $\Delta BT_{9.61\text{-}13.3}$ is another indicator of cloud top height. The 9.61 and 13.3 μm wavelengths are the ozone and CO2 absorption channels, respectively. The temperature of 9.61 μm channel is higher for high-altitude clouds because of the warming effect of ozone. Therefore, positive values of $\Delta BT_{9.61\text{-}13.3}$ represent high-level clouds, while negative values represent low-level clouds.

The $\Delta BT_{8.5\text{-}10.35}$ is used to extract information of the cloud phase and the partitioning of cloud into "water" or "ice" (Thies et al., 2008b) because water versus ice absorption differs in these two channels (Baum et al., 2000) as witnessed by a positive value for ice clouds and a small negative value for low-level water clouds. Convective precipitation is more related to ice clouds (Baum et al., 2006).

The $\Delta BT_{8.5\text{-}12.3}$ indicates the optical thickness of clouds, returning positive values for high clouds, which are relatively thick with larger particle sizes. Negative values result from low-level water clouds due to the low temperature of water vapor in 8.5 μm. The $\Delta BT_{7.34\text{-}8.5}$ also indicates the cloud optical thickness, which is adopted in the precipitation rate retrieval algorithm of ABI (Kuligowski, 2010).

Three additional parameters are selected from the ABI's VIS and NIR channels to optimize accuracy. Refs of 0.64 μm and 0.865 μm provide cloud brightness. Clouds with higher reflectance in the VIS bands tend to have more water or ice contents, which

potentially results in more rainfall and vice versa (Nakajima and Nakajma, 1995). And Ref of 2.24 μm reflects the LWP.

Section Three Methodology

4.3.1. Data processing

The goals of the automatic rainy cloud monitoring system are to detect the rainy area and delineate the convective areas. These two goals are met through the following steps:

1.   Data preprocessing. First, the 16 bands of ABI radiance are gridded to the spatial resolution of 0.1°, the same as IMERG precipitation estimates. Second, six individual ABI data with scanning time ranges included in one IMERG time step are averaged to complete the spatial and temporal collocation between the two datasets. Third, Ref, BT, and Sun Zenith angle (z) are calculated with Reflectance being derived as follows (Equation (**8**):

$$\mathbf{Ref}_\lambda = \mathbf{L}_\lambda * \kappa \tag{8}$$

where λ is the central wavelength of the channel, $\mathbf{L}_\lambda$ is the radiance value, and κ is the reflectance conversion factor. The BT is derived from Equation (9) as follows:

$$\mathbf{BT} = \left[\frac{\mathbf{fk2}}{\mathbf{alog}\left(\frac{\mathbf{fk1}}{\mathbf{L}_\lambda} + \mathbf{1}\right)} - \mathbf{bc1} \right] / \mathbf{bc2} \tag{9}$$

where fk1, fk2, bc1, and bc2 are the Planck Function constants. Sun zenith angle (z) is calculated through the variables in the ABI data file and pixel locations.

2.   Spectral parameters are calculated and normalized.

3.   Each set of parameters is sorted to rainy and non-rainy clouds according to the associated IMERG rain rate (r). If r < 0.1 mm/hr, the sample is classified as non-rainy; otherwise, it is labeled as rainy. The rainy cloud detection models are built using DNN models, through which rainy samples are separated automatically from non-rainy ones.

$$\text{Sample} \in \begin{cases} \text{Rainy} & \text{if } r \geq 0.1 \text{ mm/hr} \\ \text{Non-rainy} & \text{if } r < 0.1 \text{ mm/hr} \end{cases}$$

4.   After rainy or non-rainy samples are distinguished, the convective and stratiform rain clouds are split based on their rain rates. The adopted threshold to discriminate convection or stratus cloud is calculated through the Z-r relation (Hunter, 1996) as shown in Equation 10:

$$Z = 300r^{1.4} \tag{10}$$

$$\text{dBZ} = 10 * \log_{10} Z$$

where Z ($mm^6 \, m^{-3}$) is the reflectivity factor of the radar, r (mm/hr) is the correspondent rain rate, and dBZ is the decibel relative to Z. Lazri (Lazri, 2014) uses dBZ = 40 as the threshold of Z for convective precipitation. Then r is 12.24 mm/hr according to equation (4). As precipitation rates measured by meteorological radar tend to be overestimated due to anomalous propagation of the radar beam (Islam, 2012), a lower threshold for r is more reasonable. This research uses r=10 mm/hr as the final threshold because it is adopted frequently and has worked well in previous studies (Baquero et al., 2005; Maeso et al., 2005):

$$\text{Sample} \in \begin{cases} \text{Convective} & \text{if } r \geq 10 \text{ mm/hr} \\ \text{Stratiform} & \text{if } r < 10 \text{ mm/hr} \end{cases}$$

5.	Convective precipitation delineation models are built using training samples derived from step 4 with DNN models.

6.	Accuracy is evaluated using validation data and case studies.

A flow chart of this procedure is illustrated in **Figure 11**.
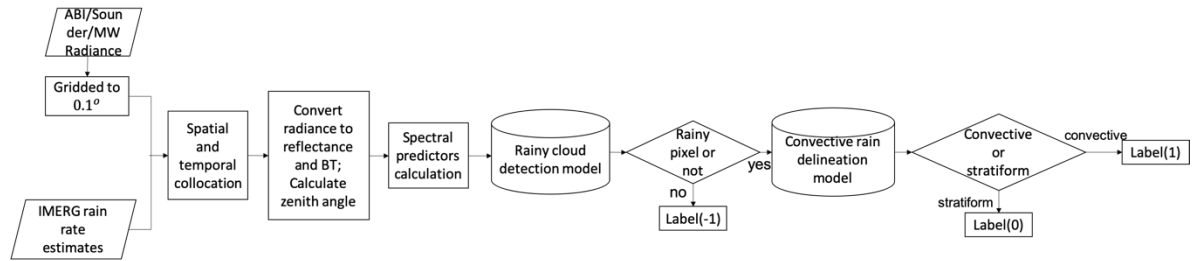
Figure 11. Workflow of the automatic rainy cloud classification system

4.3.2. *Model development*

Following the data processing steps, the classification system contains two types of models: the rainy area detection and convective precipitation delineation models. This research adopts DNN methods to build both types of models and compares the performance with SVM and RF methods.

The DNN is a feed-forward artificial neural network with multiple hidden layers between the input and output (Qian et al., 2014). The schematic workflow of the proposed DNN model (Figure 3) depicted in the input, hidden, and output layers forming a bipartite structure with all these layers fully connected. The goal of this research is to detect the rainy cloud pixels and further classify them into two classes for each step. The DNN estimates the posteriors of each class given the input cloud features x which refer to the spectral parameters. The activation functions used in each neuron of the hidden layers are Rectified Linear Units (ReLUs) function, which has the following advantages: 1) faster computation; and 2) more efficient gradient propagation (Dahl et al., 2013). The output is computed via the normalized exponential function to force the target label to have the maximum posterior estimation. The objective is to minimize the cross-entropy between the predictions of DNN p = $[p_1, p_2, \ldots p_J]^T$ and the target probabilities d = $[d_1, d_2, \ldots, d_J]^T$ (Xu et al., 2016). The loss function is defined in Equation (11):

$$L = -\sum_{j=1}^{J} d_j * \log(p_j) \tag{11}$$

The back-propagation (BP) algorithm (Hinton et al., 2012) is adopted to update the weights and bias of DNN based on the calculated loss.

The models achieve the optimal results when three hidden layers are embedded, and the numbers of neurons are 30, 20, and 20 for each hidden layer. For the rainy cloud detection models, 'Yes' is returned when the pixel is identified as rainy and 'No' for non-rainy. For the convective area, delineation models 'Yes' is returned for convective pixels

57

and 'No' for stratiform. In applications, the non-rainy, stratiform, and convective pixels are labeled as -1, 0, and 1 in series.
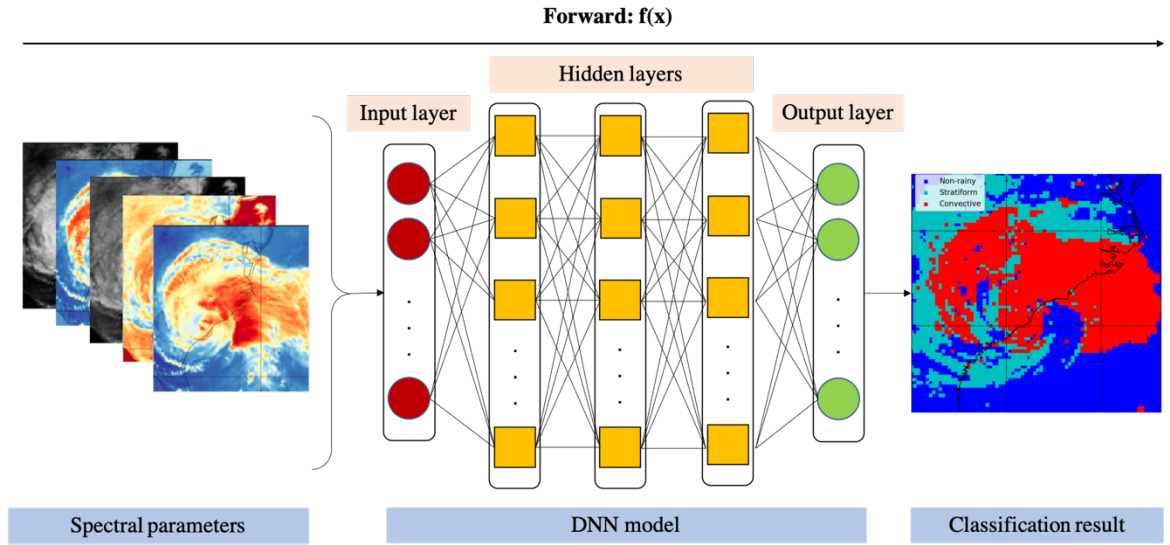
Figure 12. Flowchart of DNN model for cloud classification and delineation

<u>Section Four Model Performance Evaluation</u>

To include enough rainy and convective samples, training data are selected during rainy days from June to September of 2018, which contain at least one precipitation event in each date and have a large ensemble of different rain conditions. Eleven rainy days are

selected as testing samples that do not overlap with training events (**Table 5**). Samples are randomly split into training (70%) sets and validation (30%) sets. The total number of pixels is 1,044,072.

Table 5. Dates of precipitation events in training and testing data

Training and validation samples	Testing samples
3-5,17, 22 June;	1, 10, 24 June;
4, 7, 30-31 July;	11, 26 July;
2-4, 8-12, 18-20, 22 August;	5-7 August;
7-8,14,17, 25 September	4-6 September

4.4.1. Evaluation metrics

Table 6. Contingency parameters of the statistical assessors.

	By IMERG	
	Yes	No (Non-

		(Rainy/Convective)	rainy/Stratiform)
	Yes (Rainy/Convective)	a	b
By models	No (Non-rainy/Stratiform)	c	d

This research uses the following statistical assessors to evaluate model accuracy, which are calculated in Equations (12)-(17):

1.   The probability of detection (POD). The POD is the rate of testing samples correctly recognized as rainy/convective by the model:

$$POD = \frac{a}{a+c} \tag{12}$$

2.   The probability of false detection (POFD). The POFD indicates the fraction of rainy/convective events incorrectly predicted by the model:

$$POFD = \frac{b}{b+d} \tag{13}$$

3.   The False Alarm Ratio (FAR). The FAR is the ratio of the incorrect detection of rainy/convective pixels and the total pixels recognized as rainy/convective:

$$FAR = \frac{b}{a+b} \tag{14}$$

4.   The bias. Bias represents model over- or underestimates of reality:

$$Bias = \frac{a+b}{a+c} \tag{15}$$

5.   The Critical Success Index (CSI). The CSI is the fraction between the correct prediction of rainy/convective pixels by the model and the total number of pixels detected as rainy/convective by both IMERG and the model:

$$CSI = \frac{a}{a+b+c} \tag{16}$$

6.   The Model Accuracy (MA). The MA is the probability of a correct prediction of both rainy/convective and non-rainy/stratiform pixels by the model:

$$MA = \frac{a+d}{a+b+c+d} \tag{17}$$

where the contingency parameters a, b, c, and d are summarized (**Table 6**).

4.4.2. Comparison of DNN, SVM, and RF performance on testing data

According to the assessors' accuracies, the DNN system correctly detected most of the rainy areas (POD = 0.86 and CSI = 0.71) and convective areas (POD = 0.72 and CSI = 0.58) with relatively high overall accuracies (0.87 and 0.74, respectively). The research compared the performance of the DNN method with other two machine learning methods, SVM and RF, and found that DNN performs better on the testing sets, especially in the delineation of convective precipitation.

For rainy area detection (**Table 7**), all three methods slightly overestimate the rainy pixels, while DNN achieved the highest accuracy in all the assessors. Overall the performance of the three methods is similar, with no more than a 0.03 difference.

Table 7. Validation of rainy cloud detection model on testing data. The best

result for each assessor is shown in bold.

Model	POD (ideal 1)	POFD (ideal 0)	FAR (ideal 0)	Bias (ideal 1)	CSI (ideal 1)	MA (ideal 1)
DNN	**0.86**	**0.13**	**0.20**	**1.07**	**0.71**	**0.87**
SVM	0.85	**0.13**	0.21	**1.07**	0.69	0.86
RF	0.85	0.14	0.21	1.09	0.70	0.86

For convective precipitation delineation (**Table 8**) the advantage of DNN is even more evident, but all models overestimated the convective areas except the DNN model. The DNN achieves the highest accuracy for almost all the assessors except POD (0.72 vs. 0.86 and 0.78). The DNN performed much better than RF and SVM with a 0.20 lower FAR and 0.07~0.09 higher CSI. The SVM and RF significantly overestimated the convective pixels with FAR larger than 0.40.

Table 8. Validation of convective precipitation delineation model on testing

data. The best result for each assessor is shown in bold.

Model	POD (ideal 1)	POFD (ideal 0)	FAR (ideal 0)	Bias (ideal 1)	CSI (ideal 1)	MA (ideal 1)
DNN	0.72	**0.23**	**0.24**	**0.94**	**0.58**	**0.74**
SVM	**0.86**	0.40	0.44	1.55	0.51	0.69
RF	0.78	0.35	0.43	1.37	0.49	0.70

The errors are mainly introduced by two sources. First, the acquisition time and frequency are different for ABI images and IMERG estimations. There are differences and gaps in scanning periods between ABI and the instruments used in IMERG data, precipitation distribution, and density may change and evolve in the period. Second, since the ABI data have 0.5, 1, and 2 km spatial resolutions originally and are gridded to 0.1°, the spatial coverage is not the same for each set of spectral parameters and their associate rain rate. Errors also occur in the averaging process for spatial-temporal collocation.

Overall, the classification system efficiently detected the rainy area and extracted the convective areas from the testing dataset. In addition, most of the highest accuracies were observed in the proposed DNN models, being better performers than traditional machine learning when the data are complicated and sparsely distributed with a relatively large

size (Caruana and Niculescu-Mizil, 2006). The training and testing sample sizes are more than 500,000 and 50,000; on the other hand, there are 15 spectral parameters for each pixel with different values.

Section Five Case study

Two case studies, a normal one and an extreme precipitation one (Hurricane Florence in 2018), are used to validate the performance of the classification system. Validation is carried out using only the DNN method due to its superior performance.

4.5.1. Normal precipitation events

The comparisons are shown between the predictions of the system and IMERG estimation of normal precipitation events for July 9, 2018 (**Figure 13**). The system accurately detects the rainy and convective area but slightly overestimates both. One possible reason is the temporal difference between the IMERG estimates and the ABI predicted results. The ABI data are temporally averaged from 13:30~14:00 UTC, whereas the IMERG data are retrieved at 14:00 UTC. Another reason is that the samples used in the training dataset are insufficient, which could be improved with the accumulation of the ABI data. Lastly, the thresholds that determine rainy clouds are arbitrary, resulting in biases to their intercomparison result. Despite this shortcoming, the spatial distribution patterns of the predicted result and the IMERG data are congruent.

a)   b)
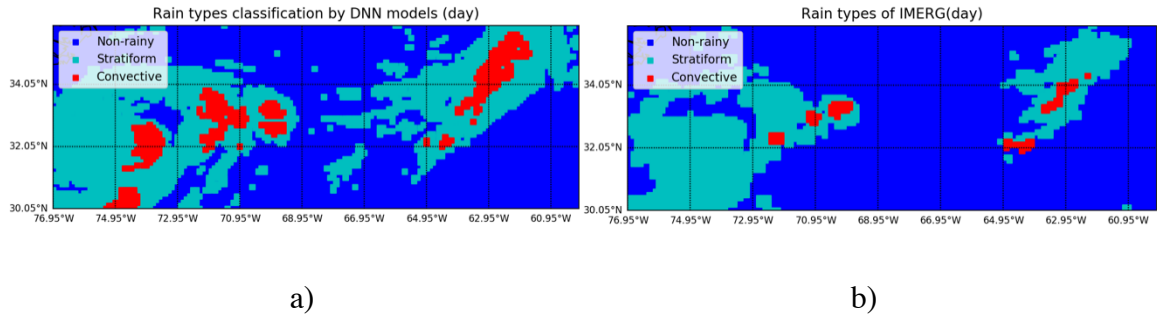
Figure 13. Cloud classification results and IMERG estimations on normal precipitation: a) ABI Prediction; and b) IMERG estimation on July 9, 2018, at 13:30~14:00 UTC.

The results of a second case study of a normal precipitation event (September 9, 2018) show the system effectively identified the rainy areas and convective areas with a minor underestimation on the rainy area and a minor overestimation on the convective areas (Figure 5).
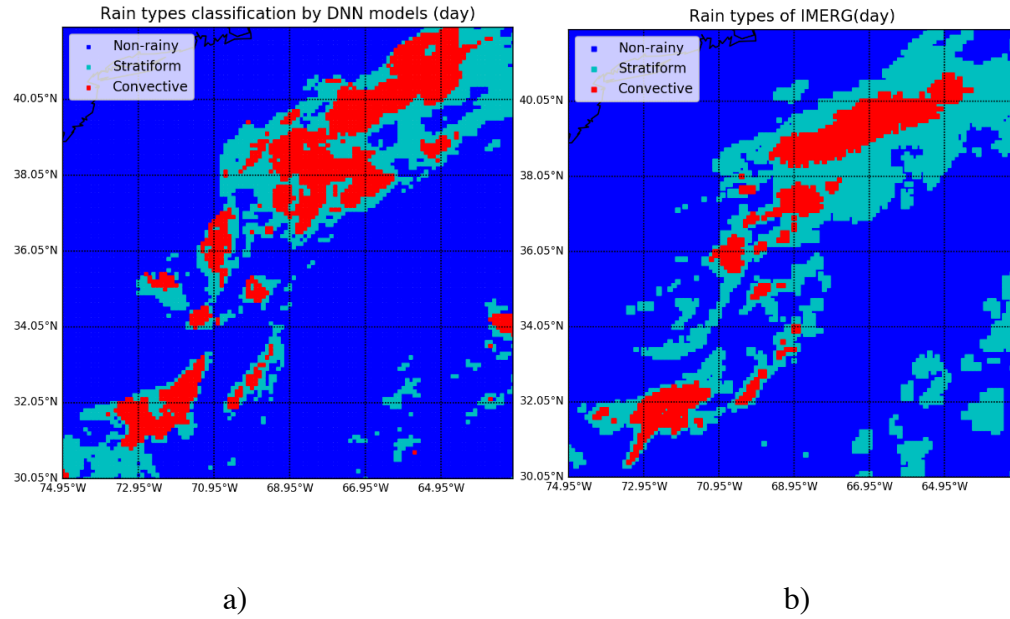
Figure 14. Cloud classification results and IMERG estimations on normal
precipitation: a) ABI Prediction; and b) IMERG estimation on September 19,
2018, at 18:00~18:30 UTC.

4.5.2. Hurricane Florence

The comparisons between the predictions of the system and IMERG estimations of
Hurricane Florence demonstrate that the system detected most of the rainy areas, and the
results clearly show the hurricane's shape and area of influence (Figure 6). For the
convective precipitation delineation, the models identify almost all the convective areas.

The system accurately detected the convective areas over the ocean with a slight overestimation and missed some pixels over land. Overall, the system performs better over the ocean than land in the Hurricane Florence case study. Precipitation on the land is influenced by more factors than that over the ocean, including topography, land use, and vegetation (Rodgers et al., 1979). The precipitation estimations of IMERG were calibrated by ground-based rain gauge data, and the measurements differ from those of the satellite-based system. In addition, different from normal precipitation events, hurricanes are extreme events where the clouds having more complicated air motion in both the horizontal and vertical dimensions. However, as most samples used to train the models are normal precipitation, Florence is the only hurricane event during the available period of ABI data in the study area. It is proposed that the models do not learn well about extreme events through the current data source.

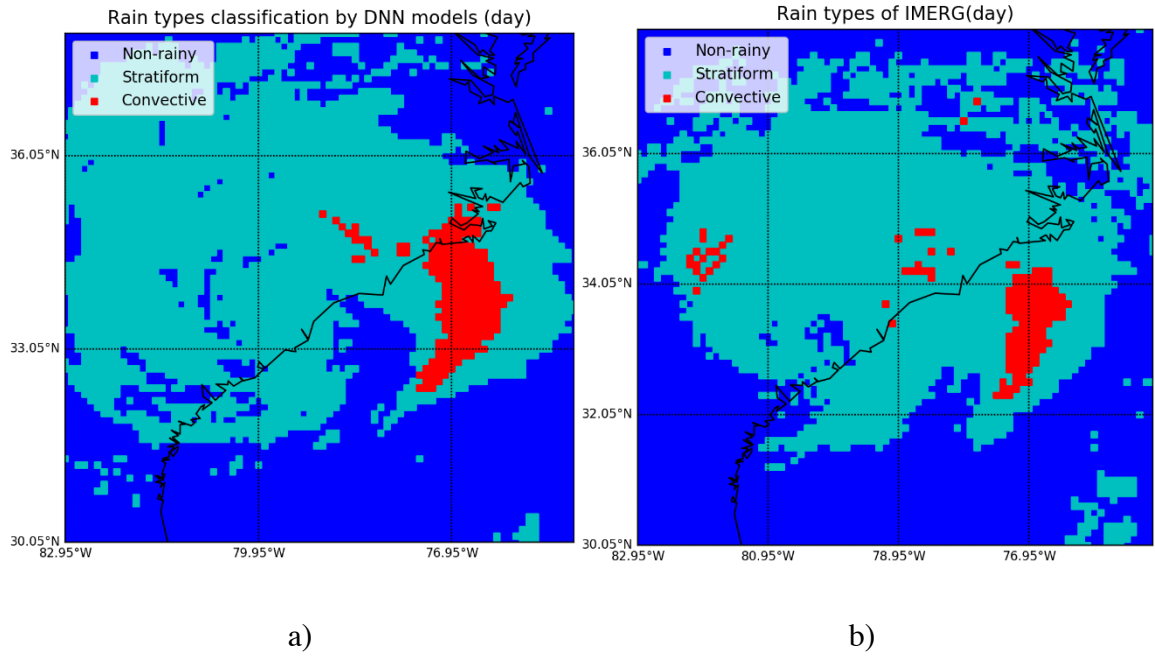Rain types classification by DNN models (day)

Rain types of IMERG(day)

a)

b)

Figure 15. Cloud classification results and IMERG estimations of Hurricane

Florence: a) ABI; and b) IMERG estimation on September 15, 2018, at

18:00~18:30 UTC.

Section Six Discussion

This research explores the performance of rainy cloud detection and convective

precipitation delineation based on GOES-ABI data using the DNN method. The system

detected the rainy cloud with relatively high accuracy and is reliable in the convective

68

area extraction. However, overestimation is observed in the identification of convective precipitation, especially over land areas.

Due to the limitations of passive instrumentation, one of the recognized weaknesses in extracting cloud information from brightness temperature is that it only provides the vertical column-integrated cloud information. Although the spectral parameters adopted in this research were effective in reflecting the information of LWP by using the differences of BTs, they do not measure raindrops in the cloud directly as done by the PMW data. Therefore, the IR-BTD based method does not perform well enough in deciding the rain rates. Overestimation of convective rain areas occurred in the validations and case studies.

However, the ABI data surpasses the PMW data in both spatial and temporal resolution and provides real-time monitoring and detection. The ABI's temporal resolution is 5 minutes, and after the system is constructed, classification results are produced in the same interval. Conversely, the temporal resolution of IMERG is 30 minutes, six times less frequent than ABI. The system provides rainy cloud classification results in a spatial resolution of 2 km, five times greater than that of the IMERG data. It functions in the prediction of convective precipitation in both urgent precipitation hazards and routine weather forecasts and is an alternative when PMW data are unavailable.

Radar-based QPE offers a high-quality estimation of precipitation. However, ground-based radar is sparsely distributed and not available over the ocean, which has a high percentage of the heavy precipitation events (i.e., open ocean) and areas with the most significant economic impact (i.e., coasts). The GOES-ABI has a full and continuous

coverage of northern and southern America and large areas of the ocean. The system proposed herein complements the Radar-based QPE over areas in which ground-based radar is unavailable.

To improve the performance of the proposed automatic detection system, several initiatives are envisioned. First, more spectral information is needed, primarily reflecting the features inside the clouds. This could be accomplished by adding an IR sounder, Microwave images, and re-analysis of data like ECMWF (European Centre for Medium-Range Weather Forecasts) and MERRA2 (Modern-Era Retrospective analysis for Research and Applications, Version 2). The second is better quality control in selecting rainy and convective pixels for training models. This is addressed by adding more thresholds to the spectral parameters to further filter errors and bias. The third is that to distinguish stratiform and convective precipitation using solely a fixed precipitation rate is quite arbitrary. This is addressed by including more variables (e.g., pressure and temperature). The fourth is to extend the research to precipitation rate estimation and introduce AI methods, especially DL, to the transformation of statistical knowledge about meteorological phenomena into numerical models. This helps improve the accuracy of numerical weather predictions (NWP). The fifth is that the precipitation product of Next Generation Weather Radar (NEXRAD) needs to be considered as validation data. The sixth focuses on the cloud types and precipitation conditions that differ under other climate regimes (Berg et al., 2002). The models and system constructed in this research address only the daytime of the East Coast of the U.S. Future investigations need to

address separate classification systems for different areas of the U.S. and those happening

during the nighttime.

CHAPTER FIVE CONCLUSIONS AND FUTURE WORK

Section One Cloud Fraction Retrieval

While cloud fraction information is critical for climate models as well as various meteorological applications, an efficient cloud fraction retrieval method is still needed. Therefore, this paper proposes a novel cloud fraction retrieval framework by leveraging the state-to-art AI deep neural network models, to estimate the cloud fraction within a single FOV of the infrared hyperspectral sounder (CrIS) at high efficiency and automation. Through analysis of model performance on a test dataset covering all seasonal conditions and several other individual use cases, the proposed model is proven to accurately retrieve cloud fraction under different spatiotemporal domains.

In general, the model achieves a high cloud fraction retrieval accuracy, with a low MSE of 0.02 and high R of 0.924, as compared with the truth calculated from the VIIRS cloud mask. Moreover, the model tends to have better results during daytime than nighttime with MSE values of 0.014 vs 0.030. The better performance in the daytime is because the signal received by the instrument in the daytime is much stronger than that of the nighttime, enabling both the CrIS and VIIRS to capture more information of the clear sky as well as cloud features, and thus making their spectra are much easier to be distinguished during the daytime. Furthermore, the model performs better over ocean than land with MSE values of 0.017 vs 0.033, which can be attributed to simpler surface

coverage and less signal disturbance from the surrounding environment. The DNN model overestimates the cloud fraction over areas with low cloud coverage and underestimates those over areas with high cloud coverage. This is because the relationship between the model predictors (CrIS spectra) and the cloud fraction values is nonlinear. In addition, larger uncertainty is observed over thin cloudy areas, possibly since the spectra of clear sky and thin cloud are similar with each other, making it hard for the model to correctly predict these two scenarios. Moreover, a lower model accuracy is also observed over high-latitude regions covered by snow or ice. The main explanation for this is that the accuracy of VIIRS cloud mask is relatively low over these areas, therefore, reducing the model's ability to retrieve cloud fraction over these areas.

Following the work presented in this paper, future work will focus on improving the following aspects to increase the model's performance:

1). Improving the training dataset. More training data will be added such that the experiments are more representative of the many global atmospheric and surface states. In addition, the CrIS and VIIRS data has been reprocessed with optimal algorithms through their life cycle recently (Zou et al., 2020; Chen et al., 2021), and both the accuracy of both datasets has been improved. Therefore, the model will be retrained with updated data in the near future to see if its performance can be further improved.

2). Improving the model. First of all, more sensitivity tests will be conducted to tune the parameters and optimize the model, such as the use of a more complex neural network during training or different combinations of neurons, PC numbers and epochs. Additionally, the model will be trained under different situations so that the model

performance will be improved over low accuracy areas. This can be achieved, for example, by training the model for land, ocean, daytime, and nighttime scenarios separately.

3). Focusing on improving the model performance of partially thin clouds which is hard to be distinguished from clear-sky pixels.

4). Exploring the object-based methods such as CNN using the morphological characteristics of clouds.

Lastly, the methodology described in this study can be easily adapted to other similar instruments (such as AIRS and IASI). Additionally, this methodology can be utilized for other non-hyperspectral satellite instrument pairs as well, provided that the lower and higher spatial resolution instruments could be accurately collocated together in a similar way as described in this paper. The retrieval model detailed in this paper can be particularly useful in partial cloud detection. Currently, the infrared sounder data serving in NWPs and GCMs can be classified as clear sky or cloudy, whereas partially cloudy scenes are undeterminable. However, this information is crucial for climate models, as the influence of partially cloudy scenes produces very different radiative forcing effects of the atmosphere than that of totally cloudy scenes. Further investigation of the partial cloud detection method could promote the application of the proposed cloud retrieval methodology in an operational mode for various applications, such as big spatiotemporal remote sensing data analytics and prediction accuracies improvement for GCMs and NWPs.

Section Two Rainy Cloud Classification

This research explores the performance of rainy cloud detection and convective precipitation delineation based on GOES-ABI data using the DNN method. The system detected the rainy cloud with relatively high accuracy and is reliable in the convective area extraction. However, overestimation is observed in the identification of convective precipitation, especially over land areas.

Due to the limitations of passive instrumentation, one of the recognized weaknesses in extracting cloud information from brightness temperature is that it only provides the vertical column-integrated cloud information. Although the spectral parameters adopted in this research were effective in reflecting the information of LWP by using the differences of BTs, they do not measure raindrops in the cloud directly as done by the PMW data. Therefore, the IR-BTD based method does not perform well enough in deciding the rain rates. Overestimation of convective rain areas occurred in the validations and case studies.

However, the ABI data surpasses the PMW data in both spatial and temporal resolution and provides real-time monitoring and detection. The ABI's temporal resolution is 5 minutes, and after the system is constructed, classification results are produced in the same interval. Conversely, the temporal resolution of IMERG is 30 minutes, six times less frequent than ABI. The system provides rainy cloud classification results in a spatial resolution of 2 km, five times greater than that of the IMERG data. It functions in the prediction of convective precipitation in both urgent precipitation hazards and routine weather forecasts and is an alternative when PMW data are unavailable.

Radar-based QPE offers a high-quality estimation of precipitation. However, ground-based radar is sparsely distributed and not available over the ocean, which has a high percentage of the heavy precipitation events (i.e., open ocean) and areas with the most significant economic impact (i.e., coasts). The GOES-ABI has a full and continuous coverage of northern and southern America and large areas of the ocean. The system proposed herein complements the Radar-based QPE over areas in which ground-based radar is unavailable.

To improve the performance of the proposed automatic detection system, several initiatives are envisioned. First, more spectral information is needed, primarily reflecting the features inside the clouds. This could be accomplished by adding an IR sounder, Microwave images, and re-analysis of data like ECMWF (European Centre for Medium-Range Weather Forecasts) and MERRA2 (Modern-Era Retrospective analysis for Research and Applications, Version 2). The second is better quality control in selecting rainy and convective pixels for training models. This is addressed by adding more thresholds to the spectral parameters to further filter errors and bias. The third is that to distinguish stratiform and convective precipitation using solely a fixed precipitation rate is quite arbitrary. This is addressed by including more variables (e.g., pressure and temperature). The fourth is to extend the research to precipitation rate estimation and introduce AI methods, especially DL, to the transformation of statistical knowledge about meteorological phenomena into numerical models. This helps improve the accuracy of numerical weather predictions (NWP). The fifth is that the precipitation product of Next Generation Weather Radar (NEXRAD) needs to be considered as validation data. The

sixth focuses on the cloud types and precipitation conditions that differ under other climate regimes (Berg et al., 2002). The models and system constructed in this research address only the daytime of the East Coast of the U.S. Future investigations need to address separate classification systems for different areas of the U.S. and those happening during the nighttime.

This research proposes an automatic system of cloud classification based on the precipitation-producing capability to detect rainy clouds and delineate convective precipitation in real-time, based on DNN technologies. The proposed DNN model returns better accuracies on the validation dataset, especially for the convective precipitation delineation.

From the experiments and analysis, this research offers the following conclusions:

1). In the detection of rainy areas, the system provides reliable results of normal precipitation events and precipitation extremes such as hurricanes with a tendency toward overestimation;

2). The DNN achieves better performance than the two ML methods with higher accuracies of the assessors on testing data;

3). The system performs better over the ocean versus land; and

4). This study is offered as a contribution to combine the advantage of AI methodology with the modeling of atmospheric phenomena, a relatively innovative domain needing more exploration. More specifically, the system combines DNN-classifier and spectral features of rainy clouds to investigate precipitation properties. This research establishes an essential step with which to estimate precipitation rates further.

REFERENCES

Adler, R.F. and Negri, A.J., 1988. A satellite infrared technique to estimate tropical convective and stratiform rainfall. Journal of Applied Meteorology and Climatology, 27(1), pp.30-51.

Arai, K., 2016. Thresholding Based Method for Rainy Cloud Detection with NOAA/AVHRR Data by Means of Jacobi Itteration Method. International Journal of Advanced Research in Artificial Intelligence , 5(6), pp. 21-27.

Aumann, H.H., Manning, E., Barnet, C., Maddy, E. and Blackwell, W., 2009, August. An anomaly correlation skill score for the evaluation of the performance of hyperspectral infrared sounders. In Atmospheric and Environmental Remote Sensing Data Processing and Utilization V: Readiness for GEOSS III (Vol. 7456, p. 74560T). International Society for Optics and Photonics.

Alfieri, L. and Thielen, J., 2015. A European precipitation index for extreme rain-storm and flash flood early warning. Meteorological Applications, 22(1), pp.3-13.

Agostinelli, F., Hoffman, M., Sadowski, P. and Baldi, P., 2014. Learning activation functions to improve deep neural networks. arXiv preprint arXiv:1412.6830.

Antun, V., Renna, F., Poon, C., Adcock, B. and Hansen, A.C., 2020. On instabilities of deep learning in image reconstruction and the potential costs of AI. Proceedings of the National Academy of Sciences, 117(48), pp.30088-30095.

Arking, A. and Childs, J.D., 1985. Retrieval of cloud cover parameters from multispectral satellite images. Journal of Applied Meteorology and Climatology, 24(4), pp.322-333.

Bretherton, C.S., Blossey, P.N. and Khairoutdinov, M., 2005. An energy-balance analysis of deep convective self-aggregation above uniform SST. Journal of the atmospheric sciences, 62(12), pp.4273-4292.

Benz, A. et al., 2018. GOES-R SERIES DOCUMENTS. Available at: https://www.goes-r.gov/downloads/resources/documents/GOES-RSeriesDataBook.pdf. (Accessed on 3 8 2019).

Baum BA, Soulen PF, Strabala KI, King MD, Ackerman SA, Menzel WP, Yang P (2000) Remote sensing of cloud properties using MODIS airborne simulator imagery during SUCCESS: 2. Cloud thermodynamic phase. J Geophys Res 105(11):781–11, 792

Baum BA, Platnick S (2006) Introduction to MODIS cloud products. In: Qu JJ, Gao W, Kafatos M, Murphy RE, Salomonson VV (eds) Earth science satellite remote sensing: science and instruments. Springer, New York.

Baquero, M., Cruz-Pol, S. & Chandrasekar, V. B. V., 2005. Rain-rate estimate algorithm evaluation and rainfall characterization in tropical environments using 2DVD, rain gauges and TRMM data. s.l., Geoscience and Remote Sensing Symposium, 2005. IGARSS '05. Proceedings. 2005 IEEE International. Volume: 2.

Berg, W., Kummerow, C. and Morales, C.A., 2002. Differences between east and west Pacific rainfall systems. Journal of climate, 15(24), pp.3659-3672.

Campoy, A., Ducharne, A., Cheruy, F., Hourdin, F., Polcher, J. and Dupont, J.C., 2013. Response of land surface fluxes and precipitation to different soil bottom hydrological conditions in a general circulation model. Journal of Geophysical Research: Atmospheres, 118(19), pp.10-725.

Chuang, C.C., Kelly, J.T., Boyle, J.S. and Xie, S. (2012) Sensitivity of aerosol indirect effects to cloud nucleation and autoconversion parameterizations in short-range weather forecasts during the May 2003 aerosol IOP. Journal of Advances in Modeling Earth Systems, 4, M09001. https://doi.org/10.1029/2012MS000161.

Christopher, D. B., Divakarla, M., Gambacorta, A., Iturbide-Sanchez, F., Nalli, N. R., Pryor, K., Tan, C., Wang, T., Warner, J., Zhang, X., and Zhu, T. (2021) NOAA Unique Combined Atmospheric Processing System (NUCAPS) Algorithm Theoretical Basis Document, Version 3.0. Available at: https://www.star.nesdis.noaa.gov/jpss/documents/ATBD/ATBD_NUCAPS_v3.1.pdf. Accesses on: June 2021.

Chen, L., Yan, G., Wang, T., Ren, H., Calbó, J., Zhao, J. and McKenzie, R., 2012. Estimation of surface shortwave radiation components under all sky conditions: Modeling and sensitivity analysis. Remote Sensing of Environment, 123, pp.457-469.

Chen, Y., Iturbide-Sanchez, F., Tremblay, D., Tobin, D., Strow, L., Wang, L., Mooney, D.L., Johnson, D., Predina, J., Suwinski, L. and Revercomb, H.E., 2021. Reprocessing of Suomi NPP CrIS Sensor Data Records to Improve the Radiometric and Spectral Long-Term Accuracy and Stability. IEEE Transactions on Geoscience and Remote Sensing.

Caruana, R. and Niculescu-Mizil, A., 2006, June. An empirical comparison of supervised
learning algorithms. In Proceedings of the 23rd international conference on Machine
learning (pp. 161-168). ACM.

Cotton, W., Bryan, G. and Heever, S. v. d., 2010. Storm and Cloud Dynamics.
International Geophysics, Volume 99.

Chen, F., Sheng, S., Bao, Z., Wen, H., Hua, L., Paul, N.J. and Fu, Y., 2018. Precipitation
Clouds Delineation Scheme in Tropical Cyclones and Its Validation Using
Precipitation and Cloud Parameter Datasets from TRMM. Journal of Applied
Meteorology and Climatology, 57(4), pp.821-836.

Dahl, G.E., Sainath, T.N. and Hinton, G.E., 2013, May. Improving deep neural networks
for LVCSR using rectified linear units and dropout. In 2013 IEEE international
conference on acoustics, speech and signal processing (pp. 8609-8613). IEEE

Donald, D., 2018. What Type of Clouds Are Rain Clouds? Available at:
https://sciencing.com/type-clouds-rain-clouds-8261472.html. (Accessed 17 4 2019).

Dürr, B. and Philipona, R., 2004. Automatic cloud amount detection by surface longwave
downward radiation measurements. Journal of Geophysical Research: Atmospheres,
109(D5).

Eresmaa Reima, 2013. Imager-assisted cloud detection for assimilation of Infrared
Atmospheric Sounding Interferometer radiances. Quarterly Journal of the Royal
Meteorological Society, 140, 2342-2352.

Evans, K.F., Turk, J., Wong, T. and Stephens, G.L., 1995. A Bayesian approach to
microwave precipitation profile retrieval. Journal of Applied Meteorology and
Climatology, 34(1), pp.260-279.

Engström, A., Bender, F. A., Charlson, R. J. and Wood, R., 2015. The nonlinear
relationship between albedo and cloud fraction on near-global, monthly mean scale in
observations and in the CMIP5 model ensemble. Geophysical Research Letters
banner, 42(21), pp. 9871-9578.

Feidas, H. and Giannakos, A., 2012. Classifying convective and stratiform rain using
multispectral infrared Meteosat Second Generation satellite data. Theoretical and
applied climatology, 108(3-4), pp.613-630.

GOES-R Series Program Office, Goddard Space Flight Center, 2019. GOES-R Series
Data Book. Available at: https://www.goes-
r.gov/downloads/resources/documents/GOES-RSeriesDataBook.pdf. (Accessed on 10
12 2019).

Giannakos, A. and Feidas, H., 2013. Classification of convective and stratiform rain
based on the spectral and textural features of Meteosat Second Generation infrared
data. Theoretical and applied climatology, 113(3-4), pp.495-510.

Hamilton, K., 2006: High resolution global modeling of the atmospheric circulation. Adv.
Atmos. Sci., 23(6), 842–856, https:// doi.org/10.1007/s00376-006-0842-3.

Han, Y., Revercomb, H., Cromp, M., Gu, D., Johnson, D., Mooney, D., Scott, D., Strow,
L., Bingham, G., Borg, L. and Chen, Y., 2013. Suomi NPP CrIS measurements,

sensor data record algorithm, calibration and validation activities, and record data

quality. Journal of Geophysical Research: Atmospheres, 118(22), pp.12-734.

Han, Y. and Chen, Y., 2017. Calibration algorithm for cross-track infrared sounder full

spectral resolution measurements. IEEE Transactions on Geoscience and Remote

Sensing, 56(2), pp.1008-1016.

Hong, Y., Hsu, K.L., Sorooshian, S. and Gao, X., 2004. Precipitation estimation from

remotely sensed imagery using an artificial neural network cloud classification

system. Journal of Applied Meteorology, 43(12), pp.1834-1853.

Huang, X., Loeb, N.G. and Yang, W., 2010. Spectrally resolved fluxes derived from

collocated AIRS and CERES measurements and their application in model evaluation:

2. Cloudy sky and band-by-band cloud radiative forcing over the tropical

oceans. Journal of Geophysical Research: Atmospheres, 115(D21).

Huffman, G.J., Bolvin, D.T., Nelkin, E.J., Wolff, D.B., Adler, R.F., Gu, G., Hong, Y.,

Bowman, K.P. and Stocker, E.F., 2007. The TRMM multisatellite precipitation

analysis (TMPA): Quasi-global, multiyear, combined-sensor precipitation estimates

at fine scales. Journal of hydrometeorology, 8(1), pp.38-55.

Huffman, G.J., Bolvin, D.T. and Nelkin, E.J., 2015. Integrated Multi-satellitE Retrievals

for GPM (IMERG) technical documentation. NASA/GSFC Code, 612(2015), p.47.

Huffman, G. J. et al., 2018. NASA Global Precipitation Measurement (GPM) Integrated

Multi-satellitE Retrievals for GPM (IMERG). Available at:

https://pmm.nasa.gov/sites/default/files/document_files/IMERG_ATBD_V5.2_0.pdf.

(Accessed on 4 10 2019).

Han, Q., Rossow, W.B. and Lacis, A.A., 1994. Near-global survey of effective droplet

    radii in liquid water clouds using ISCCP data. Journal of Climate, 7(4), pp.465-497.

Hartmann, D. L., 1994. Global Physical Climatology. 2 ed. s.l.:Academic Press.

Hunter, S.M., 1996. WSR-88D radar rainfall estimation: Capabilities, limitations and

    potential improvements. Natl. Wea. Dig, 20(4), pp.26-38..

Hinton, G., Deng, L., Yu, D., Dahl, G., Mohamed, A.R., Jaitly, N., Senior, A.,

    Vanhoucke, V., Nguyen, P., Kingsbury, B. and Sainath, T., 2012. Deep neural

    networks for acoustic modeling in speech recognition. IEEE Signal processing

    magazine, 29.

Islam, T., A.Rico-Ramirez, M., Han, D. & K.Srivastava, P., 2012. Artificial intelligence

    techniques for clutter identification with polarimetric radar signatures. Atmospheric

    Research, Volume 109-110, pp. 95-113.

Jones, T.A., Koch, S. and Li, Z., 2017. Assimilating synthetic hyperspectral sounder

    temperature and humidity retrievals to improve severe weather forecasts.

    Atmospheric Research, 186, pp.9-25.

Joyce, R.J., Janowiak, J.E., Arkin, P.A. and Xie, P., 2004. CMORPH: A method that

    produces global precipitation estimates from passive microwave and infrared data at

    high spatial and temporal resolution. Journal of Hydrometeorology, 5(3), pp.487-503.

Jensenius, J., 2017. Cloud Classification. Available at:

    https://www.weather.gov/lmk/cloud_classification. (Accessed on 17 4 2019).

Joyce, R.J., Janowiak, J.E., Arkin, P.A. and Xie, P., 2004. CMORPH: A method that

produces global precipitation estimates from passive microwave and infrared data at

high spatial and temporal resolution. Journal of Hydrometeorology, 5(3), pp.487-503.

Jensenius, J., 2017. Cloud Classification. Available at:

https://www.weather.gov/lmk/cloud_classification. (Accessed on 17 4 2019).

World Meteorological Orgnization. International Cloud Atlas. Available at:

https://cloudatlas.wmo.int/clouds-supplementary-features-praecipitatio.html.

(Accessed 10 12 2019).

Kuligowski, Robert J.., 2010. GOES-R Advanced Baseline Imager (ABI) Algorithm

Theoretical Basis Document For Rainfall Rate (QPE). Available at:

https://www.star.nesdis.noaa.gov/goesr/documents/ATBDs/Baseline/ATBD_GOES-

R_Rainrate_v2.6_Oct2013.pdf.(Accessed on 4 10 2019).

Kopp, T.J., Thomas, W., Heidinger, A.K., Botambekov, D., Frey, R.A., Hutchison, K.D.,

Iisager, B.D., Brueske, K. and Reed, B., 2014. The VIIRS Cloud Mask: Progress in

the first year of S-NPP toward a common cloud detection scheme. Journal of

Geophysical Research: Atmospheres, 119(5), pp.2441-2456.

Kahn B. et al., 2014, The Atmospheric Infrared Sounder version 6 cloud products, 14,

399-426.

Koelemeijer, R.B.A., Stammes, P., Hovenier, J.W. and De Haan, J.F., 2001. A fast

method for retrieval of cloud parameters using oxygen A band measurements from

the Global Ozone Monitoring Experiment. Journal of Geophysical Research:

Atmospheres, 106(D4), pp.3475-3490.

Karbalaee, N., Hsu, K., Sorooshian, S. and Braithwaite, D., 2017. Bias adjustment of infrared-based rainfall estimation using passive microwave satellite rainfall data. Journal of Geophysical Research: Atmospheres, 122(7), pp.3859-3876.

Keefer, D.K., Wilson, R.C., Mark, R.K., Brabb, E.E., Brown, W.M., Ellen, S.D., Harp, E.L., Wieczorek, G.F., Alger, C.S. and Zatkin, R.S., 1987. Real-time landslide warning during heavy rainfall. Science, 238(4829), pp.921-925.

Li, J., Wang, P., Han, H., Li, J. and Zheng, J., 2016. On the assimilation of satellite sounder data in cloudy skies in numerical weather prediction models. Journal of Meteorological Research, 30(2), pp.169-182.

Lin, L., Zou, X. and Weng, F., 2017. Combining CrIS double CO_2 bands for detecting clouds located in different layers of the atmosphere. Journal of Geophysical Research: Atmospheres, 122(3), pp.1811-1827.

Li, J., Menzel, W.P., Sun, F., Schmit, T.J. and Gurka, J., 2004. AIRS subpixel cloud characterization using MODIS cloud products. Journal of Applied Meteorology, 43(8), pp.1083-1094.

Liu, Q., Li, Y., Yu, M., Chiu, L.S., Hao, X., Duffy, D.Q. and Yang, C., 2019. Daytime rainy cloud detection and convective precipitation delineation based on a deep neural Network method using GOES-16 ABI images. Remote Sensing, 11(21), p.2555.

Liu, Q., Xu, H., Sha, D., Lee, T., Duffy, D.Q., Walter, J. and Yang, C., 2020. Hyperspectral Infrared Sounder Cloud Detection Using Deep Neural Network Model. IEEE Geoscience and Remote Sensing Letters.

LeCun, Y., Bengio, Y. and Hinton, G., 2015. Deep learning. nature, 521(7553), p.436.

Liu, Q., Chiu, L. S., Hao, X. and Yang, C., 2019. Characteristic of TMPA Rainfall. Washington DC, AAG.

Lazri, M., Ameur, S., Brucker, J.M. and Ouallouche, F., 2014. Convective rainfall estimation from MSG/SEVIRI data based on different development phase duration of convective systems (growth phase and decay phase). Atmospheric Research, 147, pp.38-50.

Mason, D.C., Speck, R., Devereux, B., Schumann, G.J.P., Neal, J.C. and Bates, P.D., 2009. Flood detection in urban areas using TerraSAR-X. IEEE Transactions on Geoscience and Remote Sensing, 48(2), pp.882-894.

McNally, A.P. and Watts, P.D., 2003. A cloud detection algorithm for high-spectral-resolution infrared sounders. Quarterly Journal of the Royal Meteorological Society: A journal of the atmospheric sciences, applied meteorology and physical oceanography, 129(595), pp.3411-3423.

Molinari, J. and Dudek, M., 1992. Parameterization of convective precipitation in mesoscale numerical models: A critical review. Monthly Weather Review, 120(2), pp.326-344.

Milford, J.R. and Dugdale, G., 1990. Estimation of rainfall using geostationary satellite data. Applications of remote Sensing in Agriculture, pp.97-110.

Mohia, Y., Ameur, S., Lazri, M. and Brucker, J. M., 2017. Combination of Spectral and Textural Features in the MSG Satellite Remote Sensing Images for Classifying Rainy Area into Different Classes. Journal of the Indian Society of Remote Sensing, 45(5), p. 759–771.

Mueller, B., Seneviratne, S.I., Jimenez, C., Corti, T., Hirschi, M., Balsamo, G., Ciais, P., Dirmeyer, P., Fisher, J.B., Guo, Z. and Jung, M., 2011. Evaluation of global observations-based evapotranspiration datasets and IPCC AR4 simulations. Geophysical Research Letters, 38(6).

McGovern, A., Elmore, K.L., Gagne, D.J., Haupt, S.E., Karstens, C.D., Lagerquist, R., Smith, T. and Williams, J.K., 2017. Using artificial intelligence to improve real-time decision-making for high-impact weather. Bulletin of the American Meteorological Society, 98(10), pp.2073-2090.

Meyer, H., Kühnlein, M., Appelhans, T. and Nauss, T., 2016. Comparison of four machine learning algorithms for their applicability in satellite-based optical rainfall retrievals. Atmospheric Research, 169(2016), pp. 424-433 .

Maeso, J., Bringi, V., Cruz-Pol, S. & Chandrasekar, V., 2005. DSD characterization and computations of expected reflectivity using data from a two-dimensional video disdrometer deployed in a tropical environment. Seoul, South Korea, Proceedings. 2005 IEEE International Geoscience and Remote Sensing Symposium, 2005. IGARSS '05.

Nakajima, T.Y. and Nakajma, T., 1995. Wide-area determination of cloud microphysical properties from NOAA AVHRR measurements for FIRE and ASTEX regions. Journal of the Atmospheric Sciences, 52(23), pp.4043-4059.

O'Gorman P. A., 2015. Precipitation Extremes Under Climate Change. Current Climate Change Reports, 1(2), p. 49–59.

Qian, Y., Fan, Y., Hu, W. and Soong, F.K., 2014, May. On the training aspects of deep neural network (DNN) for parametric TTS synthesis. In 2014 IEEE International Conference on Acoustics, Speech and Signal Processing (ICASSP) (pp. 3829-3833). IEEE.

Ramanathan, V.L.R.D., Cess, R.D., Harrison, E.F., Minnis, P., Barkstrom, B.R., Ahmad, E. and Hartmann, D., 1989. Cloud-radiative forcing and climate: Results from the Earth Radiation Budget Experiment. Science, 243(4887), pp.57-63.

Rios Gaona, M.F., Overeem, A., Brasjen, A.M., Meirink, J.F., Leijnse, H. and Uijlenhoet, R., 2017. Evaluation of rainfall products derived from satellites and microwave links for The Netherlands. IEEE Transactions on Geoscience and Remote Sensing, 55, pp.6849-6859.

Rodgers, E., Siddalingaiah, H., Chang, A.T.C. and Wilheit, T., 1979. A statistical technique for determining rainfall over land employing Nimbus 6 ESMR measurements. Journal of Applied Meteorology, 18(8), pp.978-991.

Reid, J. S., Hobbs, P. V., Rangno, A. L. & Hegg, D. A., 1999. Relationships between cloud droplet effective radius, liquid water content, and droplet concentration for warm clouds in Brazil embedded in biomass smoke. Journal of Geophysical Research, Volume 104, pp. 6145-6153.

Rossow, W.B. and Schiffer, R.A., 1999. Advances in understanding clouds from ISCCP. Bulletin of the American Meteorological Society, 80(11), pp.2261-2288.

Scofield, R.A., 1987. The NESDIS operational convective precipitation-estimation technique. Monthly Weather Review, 115(8), pp.1773-1793.

Sherwood, S.C. and Wahrlich, R., 1999. Observed evolution of tropical deep convective

    events and their environment. Monthly Weather Review, 127(8), pp.1777-1795.

Susskind, J., Barnet, C.D. and Blaisdell, J.M., 2003. Retrieval of atmospheric and surface

    parameters from AIRS/AMSU/HSB data in the presence of clouds. IEEE

    Transactions on Geoscience and Remote Sensing, 41(2), pp.390-409.

Susskind, J., Barnet, C., Blaisdell, J., Iredell, L., Keita, F., Kouvaris, L., Molnar, G. and

    Chahine, M., 2006. Accuracy of geophysical parameters derived from Atmospheric

    Infrared Sounder/Advanced Microwave Sounding Unit as a function of fractional

    cloud cover. Journal of Geophysical Research: Atmospheres, 111(D9).

Susskind, J., Blaisdell, J.M., Iredell, L. and Keita, F., 2011. Improved temperature

    sounding and quality control methodology using AIRS/AMSU data: The AIRS

    science team version 5 retrieval algorithm. IEEE transactions on geoscience and

    remote sensing, 49(3), pp.883-907.

Susskind, J., Blaisdell, J.M. and Iredell, L., 2014. Improved methodology for surface and

    atmospheric soundings, error estimates, and quality control procedures: the

    atmospheric infrared sounder science team version-6 retrieval algorithm. Journal of

    Applied Remote Sensing, 8(1), p.084994.

Susskind, J., Kouvaris, L., Blaisdell, J.M. and Iredell, L., 2017, December. Analysis of

    CrIS/ATMS using AIRS Version-7 Retrieval and QC Methodology. In AGU Fall

    Meeting Abstracts (Vol. 2017, pp. A12B-05).

Schmit, T.J., Griffith, P., Gunshor, M.M., Daniels, J.M., Goodman, S.J. and Lebair, W.J.,
2017. A closer look at the ABI on the GOES-R series. Bulletin of the American
Meteorological Society, 98(4), pp.681-698

Sekiguchi, M., Nakajima, T., Suzuki, K., Kawamoto, K., Higurashi, A., Rosenfeld, D.,
Sano, I. and Mukai, S. (2003) A study of the direct and indirect effects of aerosols
using global satellite data sets of aerosol and cloud parameters. Journal of
Geophysical Research, 108(D22), 4699. https://doi.org/10.1029/2002JD003359.

Smith, J.A. and Taylor, J.P., 2004. Initial cloud detection using the EOF components of
high-spectral-resolution infrared sounder data. Journal of Applied Meteorology, 43(1),
pp.196-210.

Sikma, M. and Vilà-Guerau de Arellano, J., 2019. Substantial reductions in cloud cover
and moisture transport by dynamic plant responses. Geophysical Research Letters,
46(3), pp.1870-1878.

Sihler, H., Beirle, S., Dörner, S., Gutenstein-Penning de Vries, M., Hörmann, C., Borger,
C., Warnach, S. and Wagner, T., 2020. MICRU background map and effective cloud
fraction algorithms designed for UV/vis satellite instruments with large viewing
angles. Atmospheric Measurement Techniques Discussions, pp.1-58.

Schlef, K.E., Moradkhani, H. and Lall, U., 2019. Atmospheric circulation patterns
associated with extreme United States floods identified via machine learning.
Scientific reports, 9(1), pp.1-12.

Scott Lindstrom, Tim Schmit, Jordan Gerth, 2017. GOES-R ABI Fact Sheet Band 6
("Cloud Particle Size" near-infrared). Available at:

http://cimss.ssec.wisc.edu/goes/OCLOFactSheetPDFs/ABIQuickGuide_Band06.pdf
(Accessed on 4 10 2019).

Skofronick-Jackson, G., Petersen, W.A., Berg, W., Kidd, C., Stocker, E.F., Kirschbaum, D.B., Kakar, R., Braun, S.A., Huffman, G.J., Iguchi, T. and Kirstetter, P.E., 2017. The global precipitation measurement (GPM) mission for science and society. Bulletin of the American Meteorological Society, 98(8), pp.1679-1695.

Scofield, R.A., 1987. The NESDIS operational convective precipitation-estimation technique. Monthly Weather Review, 115(8), pp.1773-1793.

Thies, B., Nauß, T. and Bendix, J., 2008. Discriminating raining from non-raining clouds at mid-latitudes using meteosat second generation daytime data. Atmospheric Chemistry and Physics, 8(9), pp.2341-2349.

Tebbi, M. A. and Haddad, B., 2016. Artificial intelligence systems for rainy areas detection and convective cells' delineation for the south shore of Mediterranean Sea during day and nighttime using MSG satellite images. Atmospheric Research, Volume 178–179, p. 380–392.

Thies, B., Nauß, T. and Bendix, J., 2008b. Precipitation process and rainfall intensity differentiation using Meteosat second generation spinning enhanced visible and infrared imager data. Journal of Geophysical Research: Atmospheres, 113(D23).

Villarini, G., Mandapaka, P.V., Krajewski, W.F. and Moore, R.J., 2008. Rainfall and sampling uncertainties: A rain gauge perspective. Journal of Geophysical Research: Atmospheres, 113(D11).

Valipour, M., 2016. Optimization of neural networks for precipitation analysis in a humid region to detect drought and wet year alarms. Meteorological Applications, 23(2016), p. 1–100.

Vijaykumar, P. et al., 2017. Distribution of cloudiness and categorization of rainfall types based onINSAT IR brightness temperatures over Indian subcontinent and adjoiningoceanic region during south west monsoon season. Journal of Atmospheric and Solar-Terrestrial Physics, 161(2017), pp. 76-82.

Wang, P., Li, J., Li, J., Li, Z., Schmit, T. J., & Bai, W. (2014). Advanced infrared sounder subpixel cloud detection with imagers and its impact on radiance assimilation in NWP. Geophysical Research Letters, 41, 1773–1780.

Wang, Z., 2018, July. The Impact of Extreme Precipitation on the Vulnerability of a Country. In IOP Conference Series: Earth and Environmental Science (Vol. 170, No. 3, p. 032089). IOP Publishing.

Wang, L., Tremblay, D.A., Han, Y., Esplin, M., Hagan, D.E., Predina, J., Suwinski, L., Jin, X. and Chen, Y., 2013. Geolocation assessment for CrIS sensor data records. Journal of Geophysical Research: Atmospheres, 118(22), pp.12-690.

Wang, L., Chen, Y. and Han, Y., 2016. Impacts of field of view configuration of Cross-track Infrared Sounder on clear-sky observations. Applied optics, 55(25), pp.7113-7119.

Wang, L., Zhang, B., Tremblay, D. and Han, Y., 2017. Improved scheme for Cross-track Infrared Sounder geolocation assessment and optimization. Journal of Geophysical Research: Atmospheres, 122(1), pp.519-536.

Wang, T., Luo, J., Liang, J., Wang, B., Tian, W. and Chen, X., 2019. Comparisons of AGRI/FY-4A cloud fraction and cloud top pressure with MODIS/Terra measurements over East Asia. Journal of Meteorological Research, 33(4), pp.705-719.

Wang, S., Liu, C., Zhang, W., Hao, N., Gimeno García, S., Xing, C., Zhang, C., Su, W. and Liu, J., 2020. Development and Application of HECORA Cloud Retrieval Algorithm Based On the O2-O2 477 nm Absorption Band. Remote Sensing, 12(18), p.3039.

World Meteorological Orgnization. International Cloud Atlas. Available at: https://cloudatlas.wmo.int/clouds-supplementary-features-praecipitatio.html. (Accessed 10 12 2019).

Wei, G., Lü, H., Crow, W.T., Zhu, Y., Wang, J. and Su, J., 2018. Comprehensive Evaluation of GPM-IMERG, CMORPH, and TMPA Precipitation Products with Gauged Rainfall over Mainland China. Advances in Meteorology, 2018.

Xu, Y., Huang, Q., Wang, W. and Plumbley, M.D., 2016. Hierarchical learning for DNN-based acoustic scene classification. arXiv preprint arXiv:1607.03682.

Yang, C., Yu, M., Li, Y., Hu, F., Jiang, Y., Liu, Q., Sha, D., Xu, M. and Gu, J., 2019. Big Earth data analytics: A survey. Big Earth Data, 3(2), pp.83-107.

Zou et al., 2020. The Reprocessed Suomi NPP Satellite Observations. Remote Sensing, 12(18), 2891, doi: 10.3390/rs12182891.

BIOGRAPHY

Qian Liu graduated from Middle School Attached to Harbin Normal University, Harbin, China, in 2005. She received her Bachelor of Engineering from Wuhan University in 2009 and received her Master of Engineering from Wuhan University in 2011.